

## BIROn - Birkbeck Institutional Research Online

Bhanot, Krishan and Downes, Hilary and Petrone, C.M. and Humpheys-Williams, E. and Clark, B. (2020) Micro-CT investigation of garnet-spinel clusters in mantle peridotite xenoliths. *Lithos* 352-3 , p. 105250. ISSN 0024-4937.

Downloaded from: <https://eprints.bbk.ac.uk/id/eprint/29597/>

*Usage Guidelines:*

Please refer to usage guidelines at <https://eprints.bbk.ac.uk/policies.html>  
contact [lib-eprints@bbk.ac.uk](mailto:lib-eprints@bbk.ac.uk).

or alternatively

# Micro-CT investigation of garnet-spinel clusters in mantle peridotite xenoliths

K.K. Bhanot <sup>a, b</sup>, H. Downes <sup>a, b</sup>, C.M. Petrone <sup>b</sup>, E. Humphreys-Williams <sup>c</sup>, B. Clark <sup>c</sup>

<sup>a</sup> Department of Earth and Planetary Sciences, Birkbeck University of London, Malet Street, London WC1E 7HX, UK

<sup>b</sup> Department of Earth Sciences, Natural History Museum, Cromwell Road, London SW7 5BD, UK

<sup>c</sup> Imaging and Analysis Centre, Natural History Museum, Cromwell Road, London SW7 5BD, UK

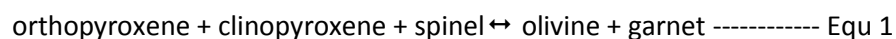
## Abstract

We have investigated the origin of garnet in garnet-spinel peridotite mantle xenoliths from two well-known localities, Pali-Aike (Patagonia) and Vitim (Siberia). We used micro-CT scanning to examine the textures of garnet-spinel clusters and the relationship between garnet and spinel. CT scanning yields different mineral modes in terms of spinel and garnet than observed in thin-section, because distribution of these phases is inhomogeneous, and a larger volume is visible in a CT scan than in a thin-section. We conclude that garnet formed after spinel in both localities, but the xenoliths record a complex tectonic history, in which the original garnets in garnet peridotites were transformed to spinel-pyroxene clusters in spinel peridotites, via lithospheric thinning. This stage was followed by deformation of the spinel peridotites, producing a lineation. A final stage of isobaric cooling caused garnet to re-grow around the spinel clusters. Aspect ratios of garnets differ from those of garnet-spinel clusters; the latter are more similar to those of spinel pyroxene clusters. Kelyphite is a secondary feature resulting from heating and rapid decompression during entrainment in the host alkali basaltic lavas and has no relationship with the formation of the garnet-spinel clusters.

Keywords: garnet-spinel peridotite; mantle xenolith; Vitim; Patagonia, CT scanning

## Introduction

Garnet-bearing peridotite mantle xenoliths are rare in off-craton alkali basaltic areas and are only reported from a few alkali basaltic provinces such as Patagonia (Skewes & Stern, 1979; Kempton et al, 1999), Siberia (Murav'yeva et al., 1987) and China (Cao & Zhu, 1987; Ionov, 2004). In studies of spinel-garnet peridotite xenoliths, Ionov et al. (1993), Ionov (2004) and Stern et al. (1999) concluded that the garnets were formed at the expense of spinel and pyroxenes in a sub-solidus reaction. This sub-solidus transition from the spinel stability field to the garnet stability field is caused by either a decrease in temperature or an increase in pressure, and is represented by the reversible equation (Smith, 1977):



This study will test the hypothesis that garnets formed from spinel and pyroxenes in suites of garnet-spinel peridotite xenoliths by using micro-CT scanning to determine their three-dimensional textures and the relationships between garnet and spinel. Micro-CT 3D volumes provide accurate and high-resolution representations of both garnet and spinel phases in peridotites. Analysis of the 3D volumes will allow comparison of garnet-spinel textures in samples from the two localities, including their aspect ratios. We will compare these with 3D textures of spinel-pyroxene clusters in spinel peridotite mantle xenoliths (Bhanot et al., 2017) which provide textural evidence of the reverse of the reaction shown in Equ 1.

### Sample localities

Our samples are from two well-known off-craton continental mantle xenolith localities: Pali-Aike (PA) in South America, and Vitim (VI) in eastern Russia. The Pali-Aike volcanic field forms part of the Patagonian plateau lavas and is  $\leq 4$  Ma in age. The western margin of South America is a convergent plate boundary between the South American, Nazca and Antarctic plates (Skewes and Stern 1979). The Pali-Aike host basalts are alkali-olivine basalts generated by partial melting of the mantle in response to tectonic changes of the South American, Nazca and Antarctic plate triple junction.

The Vitim plateau is composed of Cenozoic alkali basaltic lava flows and pyroclastic deposits, located  $\sim 250$  km east of Lake Baikal. Tectonic and geophysical studies (e.g. Petit et al., 1998) have found no evidence for large-scale lithospheric thinning beneath the Vitim plateau (Ionov, 2002). Because the Vitim

plateau is clearly distinct from the Baikal rift in terms of its relief and tectonic setting, it may be more appropriate to consider it as part of the broad diffuse area of Cenozoic alkali basaltic volcanism between the Siberian and North China cratons (Ionov 2004).

Textures and petrology of mantle xenoliths from Pali-Aike have been previously studied by Skewes and Stern (1979), Douglas et al. (1987), Stern et al. (1999), Kempton et al. (1999) and Wang et al. (2008). They are high-temperature ( $>970^{\circ}\text{C}$ ) peridotites, mostly protogranular garnet-spinel harzburgites and garnet lherzolites. Low temperature spinel peridotites were not studied. Previous studies of textures and petrology of Vitim mantle xenoliths include those of Ionov et al. (1993), Ionov (2004), Ionov et al. (2005) and Ionov and Hoffman (2007). Xenoliths from Vitim are protogranular garnet-spinel or garnet lherzolites.

### 3. Methodology

Thin-section preparation and electron microprobe analysis (EMPA) were performed at Birkbeck, University of London. The modal mineralogy was calculated by point-counting from scanned images of thin-sections. BSE images, elemental mapping and major element mineral analyses were obtained using a Jeol JXA8100 Superprobe with an Oxford Instruments Aztec energy dispersive system (EDS) at Birkbeck. EDS analysis was carried out using an accelerating voltage of 15 kV, a current of 10 nA and a beam diameter of 1  $\mu\text{m}$ . EDS analyses were calibrated against standards of natural silicates, oxides and Specpure<sup>®</sup> metals with the data corrected using a ZAF (atomic number, absorption and fluorescence) correction program.

Cylindrical cores of 25 mm diameter and approximately 25 mm length were drilled from the peridotite xenoliths for CT scanning. The shape and size of the cores were chosen to ensure equal absorption and penetration of the X-ray beam, thus reducing artefacts in the final 3D rendered CT volume. One sample (VI 313-1270) was analysed without being cored; this made little difference to the processed CT results but provided a larger volume for analysis.

Computed tomography (CT) acquires multiple sets of images of the sample over  $360^{\circ}$ . The 2D images are processed (reconstructed) to yield the raw dataset. During reconstruction, raw intensity data are converted to CT values which map linearly to the effective attenuation coefficient of the material in each voxel (Ketcham and Carlson 2001). A single tomographic slice is a cross-sectional layer of the sample and is composed of smaller divisions known as volume elements or “voxels”. In a digital image, voxel

dimensions are related to the size of a pixel and to the sum of attenuation with respect to the X-ray path. Resolution of the measurement and reconstruction is influenced by pixel size, number of pixels within each grey value profile, number of pixels or slices in the Y direction and number of angular positions (Kruth et al., 2011).

The principal configuration for CT data acquisition involves a stationary X-ray (polychromatic) source, a rotational sample stage and an X-Ray detector. The specimen is mounted on the rotating stage between the X-ray source and detector. The geometry of the specimen and X-ray source dictates the CT image resolution. By reducing the specimen-to-source distance along the magnification axis, a more magnified and better resolved image is captured at the detector, compared with a specimen at a greater distance from the X-ray source. However, higher magnification may cause blurring of the image when using a reflection target.

Since X-ray absorption is a measure of material density, its distribution within 3D images provides an insight into the internal structures and distribution of phases in a specimen. Phase analysis for 2D and 3D images is carried out by utilising the voxel intensity (grey-scale) histogram, which plots the frequency of voxels at a particular intensity and so permits the separation (segmentation) of an image into distinct phases. One major factor that must be considered when evaluating voxel intensity histograms taken from multiphase data is overlapping intensities of the different phases.

Carlson et al. (2003) reviewed the application of CT scanning in the Earth Sciences. Geological samples consist of multiple minerals of different densities and it is important to understand how such samples will react to exposure to the X-ray beam. Attenuation characteristics allow us to predict the possibility of differentiating between different minerals in CT images (Ketcham and Carlson, 2001). However, the attenuation curves for forsterite and enstatite are similar across the whole range of X-ray energies, which makes it very difficult to distinguish between these two minerals. Clinopyroxene has a higher attenuation factor at low energies (50 keV) because of the high atomic number of Ca, and so it can be distinguished in CT images. Garnet (pyrope) has a higher attenuation coefficient across the whole range of energies compared with the silicate minerals and is distinguishable in slice images. Spinel, with high density and a high linear attenuation coefficient across the whole range of energies, is easily distinguishable from the silicates. Thus, during segmentation, the garnet, spinel and silicate phases can be viewed in isolation, as can Ca-rich minerals such as clinopyroxene. With the spinel and silicate phases isolated, the 3D rendered visualisations show the grain size, shape and distribution of garnet and spinel within each rock core.

Micro-CT scans were collected at the NHM on the Metris X-Tek HMX ST 225 scanner coupled with a 4-megapixel Perkin Elmer XRD 1621 AN3 HS detector panel. The power setting for data collection for a polychromatic X-ray beam (cone beam projection) with a tungsten target (reflection target) and Cu filter (thickness 1.0 mm) was 190 kV and 210  $\mu$ A. Resolution of the 3D rendered volumes ranged from 13 to 19  $\mu$ m. The rock cores were mounted inside the X-ray enclosure and housed on a translation stage. The distance of the sample to source was set to ensure maximum magnification without introducing blurred edges. The cores were scanned with 3142 projections and an exposure time of 1000 ms.

CT scans can be affected by various artifacts which can compromise the quality of the 3D rendered volume. Beam hardening is an artefact in which the edges of an image appear more intense compared to its centre (Ramakrishna et al. 2006). To minimise this effect, we tried both Cu and Al attenuation filters with varying thickness before the X-ray beam interacted with the sample, to reduce the low energy X-rays, and found that a Cu filter with a thickness of 1 mm provided the optimum conditions.

The Avizo software suite was used for 3D segmentation and volume rendering. The data sets were analysed, segmented and rendered, and four phases were identified, i.e. air, silicate minerals, garnet and spinel. Initial data sets of garnet peridotite cores yielded data highly susceptible to beam hardening. The result was that, although the spinel was easily segmented, the garnet phase could not be accurately segmented from the other silicate phases. The scan conditions were varied in order to optimise data collection. Different X-ray tube power settings and the sample-to-source distances were tested. Although beam hardening could not be completely removed, the optimum machine conditions are as shown above. The effect of beam hardening poses a problem in segmenting similar material at the edge of the data set compared to its centre, because mean grey values for garnets at the edge appear higher than mean grey values at the centre of the 3D data set. To overcome this, the data set was cropped into a rectangular box and only the central portion was selected. A major disadvantage is that, since the large garnets are often clustered and unevenly distributed, whole garnets were often also cropped, thus reducing our ability to truly image the garnet texture. Two samples from Vitim suffered from this effect and were omitted from the data set.

Avizo has a “region-growing” utility (called a “magic wand”) in which different material can be manually selected in the individual slice images based on defined grey value range of voxels for all connected voxels, which can be assigned to that material automatically. Care must be taken that other materials are not selected and assigned incorrectly, since the attenuation coefficients for garnet are close to other silicates for samples from Vitim and Pali-Aike because of the low Cr<sub>2</sub>O<sub>3</sub> content (<2wt %) in the garnets.

Garnet and other silicate phases overlap in the 3D slice histogram and use of the region-growing can lead to errors in segmentation.

The “Volume Fraction” tool in Avizo was used to calculate the volume fraction for garnet and spinel in samples from Vitim and Pali Aike. The volume fraction tool works by comparing the number of voxels of a selected material with the total number of voxels of the sample. Volume fractions are listed in Table 1. The aspect ratio (AR) of garnets and garnet-spinel clusters were obtained from the raw 3D volume data by using ImageJ software to measure the longest and shortest axes. For comparison, the same methodology was applied to garnets in cratonic garnet peridotite xenoliths and to spinel-pyroxene clusters in xenoliths from Massif Central and Lanzarote (Bhanot et al., 2017). Videos and images of 3D volumes are available in the Supplementary data.

## Results

### Textural and modal analyses in thin-section

The modal mineralogy of the mantle xenoliths in thin-section (Table 1) shows that the samples include both garnet-spinel peridotites and garnet peridotites, but no pure spinel peridotites. All the xenoliths are coarse-grained and protogranular following the classification of Mercier and Nicolas (1975). Mineralogy consists of olivine (forsterite), orthopyroxene (enstatite), clinopyroxene (diopside),  $\pm$  spinel and garnet (pyrope). Garnet-spinel peridotites from Pali-Aike are largely harzburgites whilst those from Vitim are mostly lherzolites (Table 1). Garnet peridotites from Pali-Aike are also mostly harzburgites whereas those from Vitim are largely garnet lherzolites with one harzburgite. This suggests that samples from Pali Aike have experienced more depletion than those from Vitim. Figure 1 shows images of thin-sections of a gt lherzolite from Vitim and a gt-sp lherzolite from Pali-Aike. The samples from Vitim showed a surprising lack of spinel (Table 1).

BSE images of gt-sp peridotites and gt peridotites from both localities show coarse-grained anhedral garnets which vary in size (Fig. 2). They have irregular but generally circular grain shapes and often contain olivine inclusions. Garnets are often not randomly distributed but appear to be clustered. Spinel in gt-sp peridotites are associated with garnets and often occur as inclusions within garnets (Fig.

2a), where they form the central core surrounded by garnet. Spinel shapes vary from small blebs to large vermicular grains. The content of spinel in thin-sections of samples from Vitim is <1% whilst in those from Pali-Aike spinel content is <3% (Table 1). Garnets display no chemical zoning but are commonly mantled with a kelyphite rim (Fig. 2b) composed of garnet, cpx and spinel. Spinel and cpx grains in kelyphite rims in Vitim samples can be zoned. The contacts between garnet and spinel inclusions are also mantled with a kelyphite rim showing a similar texture to the rim surrounding the garnet.

#### *Garnet-spinel peridotites*

Garnets in garnet-spinel clusters from Vitim vary in size from <5 mm weakly elliptical to highly elliptical vermicular structures. In samples from Pali-Aike the garnet-spinel clusters are also highly elliptical, >4 mm in length and <3 mm in width, and display a vermicular texture. In thin-section, spinels vary from blebs with a mild vermicular texture inside the garnets to complex vermicular structures. Volume of spinel can vary from small individual blebs to larger complex structures forming a larger percentage of the garnet-spinel complex (PA 10).

#### *Garnet peridotites*

Garnet content in thin-sections of garnet peridotites ranges from 4 to 26% in xenoliths from Vitim and from 3 to 6% in Pali-Aike samples. Garnets in Vitim samples (Fig. 1) vary from ~2 mm rounded grains to highly elliptical vermicular grains >4 mm in length (e.g. VI 313 1278). Garnets from Pali-Aike are largely equant and approximately 2 mm in diameter (e.g. PA 18). Garnets from both locations often contain small rounded inclusions of olivine (Fig. 2b).

## Mineral chemistry

Microprobe analyses of samples from Pali-Aike (PA) and Vitim (VI) in this study (Supplementary files) are similar to previous studies from the two regions (Skewes and Stern, 1979; Stern et al., 1999; Ionov et al., 1993). Both gt-sp peridotites and gt peridotites have a similar mineral composition. Mg#s ( $Mg\# = \frac{Mg}{Mg + Fe} \times 100$ ) for olivine, orthopyroxene and clinopyroxene from the two localities are similar in the range of 88-90. Spinel Cr#s ( $Cr\# = \frac{Cr}{Cr + Al} \times 100$ ) are higher in PA samples (21–32) than in VI (19–20).  $Al_2O_3$  contents in spinel are 36-47 wt%,  $Cr_2O_3$  is 17-27 wt%, MgO is 16-20 wt% and FeO is 12-18 wt%.



206 Orthopyroxenes from both localities are enstatites with 3.5-4.4 wt%  $\text{Al}_2\text{O}_3$ . Clinopyroxenes are diopside  
207 containing 17-19 wt% CaO, 5-11 wt%  $\text{Al}_2\text{O}_3$  and <1.5 wt%  $\text{Cr}_2\text{O}_3$ . Garnets are pyrope with Mg#s 81-85.  
208 Their  $\text{Al}_2\text{O}_3$  content is 23 wt%,  $\text{Cr}_2\text{O}_3$  is 1.1 wt%, MgO is 20 wt%, CaO is 5 wt% and FeO is 8 wt%. Garnets  
209 in several samples from both localities contain olivine inclusions with Mg#s of 89-90, identical to olivines  
210 outside garnets. NiO content in both olivine inclusions inside garnets and outside garnets are also similar  
211 at <0.4 wt%.

212 Arai (1994) outlined how the values of Mg# in olivine and Cr# in spinel can constrain the origin of spinel  
213 peridotites. Spinel lherzolites and spinel harzburgites have limited ranges of  $\text{Mg\#}_{\text{olivine}}$  and  $\text{Cr\#}_{\text{spinel}}$  values,  
214 forming the olivine - spinel mantle array (OSMA). Since we have no xenoliths which are purely spinel-  
215 bearing, we have used EMPA analysis of spinel peridotites from Vitim (Ionov et al., 1995) and Pali Aike  
216 (Skewes and Stern, 1979; Wang et al., 2008) (Fig 3a). Comparing our data to previous results for spinel  
217 peridotites from the same locations, Vitim samples have higher spinel Cr#s than in spinel peridotites, but  
218 Pali Aike samples show the opposite. Ol Mg#s for VI and PA are 90 and 89, respectively. All analysed  
219 spinel Cr#s from VI and PA are much lower than those of cratonic spinel peridotite xenoliths (Fig. 3a).

220 Garnet compositions from Vitim and PA have Cr#s of 3.4-3.5 which are much lower than those of gt and  
221 gt-sp peridotites from Udachnaya (Ionov et al., 2010), Lashaine (Reid et al., 1975; Gibson et al., 2013)  
222 Kaapvaal (Carswell et al. (1979); Grégoire et al. (2003); Simon et al. (2003)) which vary from 11 to 33 (Fig  
223 3b). Mg#s of VI garnets are lower than those of PA, again suggesting that the PA samples have  
224 experienced more depletion.

225 Kelyphite rims around garnets have an average thickness of 100  $\mu\text{m}$ , which is uniform in samples from  
226 both VI and PA. Kelyphite rims display a sharp contact with garnet cores. BSE images of reaction rims  
227 arounds garnets in this study show that the kelyphite symplectite microstructures, often associated with  
228 coronae mantling garnet peridotite (Godard and Martin, 2000), are largely absent in PA and VI samples.  
229 However, one sample does show a partial portion displaying a fibrous symplectite texture. Kelyphite  
230 rims from PA and VI are composed of cpx and spinel and a secondary garnet which is more Mg-rich (Mg#  
231 85) but with lower  $\text{Al}_2\text{O}_3$  and CaO than the garnet cores. A third garnet exists in small regions in sharp in  
232 contact with the garnet core (PA 16). This garnet is more Ca-rich with 14 wt% CaO. Both Mg# (60) and  
233 Cr# (0.8) are considerably lower than the garnet core. Spinel and cpx in the kelyphite rims can be zoned  
234 (e.g. VI 313- 1278). The contact between garnet and spinel inclusions are also mantled with a kelyphite  
235 rim displaying a similar texture to the rim surrounding garnet. The presence zoning in grains in the  
236 kelyphite rim and the absence of the kelyphite texture from the cores implies that the kelyphite rim is a

secondary texture and is thus independent of the sub-solidus reaction shown in Equ 1. In fact, it is the reverse reaction ( $gt_1 + ol$  goes to  $sp + pyx + gt_2$ ) and is related to exhumation.

## Micro CT results

Modal abundances for garnet and spinel calculated from the 3D volume fraction and measured in thin-section by point counting show significant differences (Table 1). Garnet modal values from Vitim are generally higher in the micro-CT volume, but the reverse is true for samples from Pali Aike. In most cases, the spinel modal abundance is much lower in the 3D volume than in thin-section. However, in the cores of two of the Vitim xenoliths, very little garnet was found despite it being present in the thin-sections. This suggests that neither method accurately represents the actual modal abundances of these very coarse-grained rocks, but since the volume being analysed by CT-scanning is much greater than the area represented by a thin-section, the CT scans probably yield a more accurate result.

## Pali-Aike

In the Pali-Aike xenoliths, spinel is generally found in clusters with garnet, with a few exceptions in which spinels are found as individual isolated crystals. Micro-CT scans of garnet-spinel (gt-sp) clusters reveal a range of textures including (a) randomly orientated large elliptical (>2 mm) garnet grains, (b) large elliptical (>2 mm) garnet grains encasing small individual spinel blebs, (c) large (<4 mm) garnet grains encasing large complex spinel structures, (d) complex and highly elongate garnet-spinel clusters displaying a strong lineation. Distribution of garnets through the cores is often random but the garnets also occur as clusters with large volumes of the sample devoid of garnet. The individual spinel blebs form a small volume of the gt-sp cluster whereas the complex, highly vermicular spinel structures form a much higher volume of the gt-sp cluster.

The different samples from Pali-Aike show slightly different features. In PA 10, a garnet-spinel harzburgite (Fig. 4), the individual gt-sp structures vary from <10 mm in length and <2 mm in width to small gt-sp clusters <2 mm in the longest dimension. Their average AR is 2.3. Spinel forms much of the volume of these structures, whilst several spinel crystals have no associated garnet. Individual gt-sp structures often show a strong lineation (Fig. 4).

Garnet-spinel harzburgite sample PA 16 (Fig. 5) shows examples of the individual large complex gt-sp clusters displaying the ellipsoidal garnet shapes and vermicular spinel texture within the cluster. The gt-sp clusters are individual ellipsoidal structures which measure <4 mm in length and <2 mm in width, with a mean AR of 1.9. Garnet displays a vermicular texture and all spinel is associated with garnet. Spinel forms much of the volume of these structures. Spinel also forms complex and highly vermicular features enclosed within the garnet. The large complex spinel structure shows individual spinel branches which are in contact with adjacent branches, thus forming a single crystal of spinel.

Sample PA 13 (Fig. 6) is a good example where garnet grains are clustered but show no alignment. The 3D rendered volume shows much of the sample is devoid of garnet and spinel. Garnets in PA 13 are large individual grains that measure <4 mm in length and <2 mm in width, with a mean AR of 1.9. Several garnets grains are clustered in the sample core with large volumes free of both spinel and garnet. Spinel forms a low volume compared to garnet and exists as small blebs <1 mm. All spinel is associated with garnet.

Garnets in garnet harzburgite sample PA 18 (Fig. 7) are large individual grains that measure between <4 mm in length and <2 mm in width to <2 mm in diameter and are more spherical in shape (mean AR = 1.4). Garnets are randomly distributed throughout the core but regions with a higher density of garnet are visible where individual garnet grains are clustered. Spinel forms a very low volume compared to garnet and exists as small blebs <1 mm only in several grains, with most of the garnet being spinel-free. Spinel is not limited to gt-sp clusters, but several small blebs are visible in the core in garnet-free regions.

Sample PA 31 (Fig. 8) is a gt-sp peridotite. Garnet grains are randomly distributed throughout the core and vary in shape from complex vermicular grains with no spinel to spherical <4 mm size gt-sp structures (mean AR = 2.2). Large ellipsoidal spinel blebs <4 mm in size with a strong vermicular texture are not associated with garnet but are also randomly distributed throughout the core. In PA 31, garnet-free spinel blebs are surrounded by a halo of high atomic number material which is less dense than both the garnet and spinel phases (Fig. 8b). There is enough density contrast of the halo for it to be resolved from the silicate phase and is interpreted as products of metasomatic reactions similar to metasomatic halos in spinel-pyroxene clusters from Lanzarote spinel harzburgite xenoliths (Bhanot et al., 2017). This metasomatism probably accounts for the high cpx content in PA 31 (Table 1).

Vitim

Micro-CT scans of gt-sp clusters in samples from Vitim show large ellipsoidal (>2 mm) garnet grains encasing individual spinel blebs and large (<4 mm) garnet grains enveloping complex spinel structures with a strong vermicular texture. Distribution of garnets through the cores is random but the garnets are often clustered such that large volumes of the core are devoid of garnet, as in the Pali-Aike samples. Also, like samples from Pali-Aike, individual spinel blebs form a small volume of the gt-sp cluster whilst the complex, high vermicular spinel structures form a higher volume of the complex. The large complex spinel structures are ellipsoidal and individual spinel branches are in contact with adjacent branches, thus forming a single crystal of spinel.

Garnet lherzolite VI 313 1270 was the only sample that was CT-scanned without being cored and so it provided the largest imaged volume of any studied xenolith. It is also the only sample which did not contain any spinel in the 3D scan (Table 1). Fig. 9a shows that the garnets are large individual grains that measure between <4 mm in length and <2 mm in width to <2 mm in diameter and are more spherical (mean AR = 1.3). Garnets are randomly distributed throughout the core but regions with a higher density of garnet are visible where individual garnet grains are clustered.

Modal mineralogy based on thin-section analysis revealed sample VI 313 532 to be a gt lherzolite. However, analysis of the 3D volume revealed the presence of gt-sp clusters. Spinel forms a low volume compared to garnet and exists as blebs <5 mm and complex, vermicular structures with an ellipsoidal shape. Spinel is not limited to gt-sp clusters, but several small blebs (<1 mm) are also visible. Garnets in garnet-spinel peridotite VI 313 532 (Fig. 9b) are large individual ellipsoidal grains that measure <5 mm in length and <4 mm in width. Garnets are randomly and evenly distributed throughout the core. There is no spinel visible in the scan of the core of this sample, although some had been found in thin-section (Table 1).

Mean ARs for garnet in gt peridotites from Vitim and Pali-Aike are between 1.2 and 1.4. In contrast, garnets from gt-sp peridotites display a broader range of mean ARs ranging from 1.7 to 2.3. Mean ARs for gt and gt-sp peridotites are shown in Fig. 10, where they are compared to ARs for cratonic garnet peridotites and in spinel-pyroxene clusters in spinel peridotite xenoliths.

## Discussion

### *Modal abundances of garnet and spinel*

CT-scanning produces 3D volumes of gt-sp and gt peridotite xenoliths which may offer a more accurate classification of samples. Calculating modal mineralogy from thin-sections alone may not provide the most accurate classification since clustering of garnets can lead to sections of the sample being devoid of garnet. Also, gt-sp clusters can co-exist with spinel-free garnets and some samples contain no interstitial spinel. Therefore, analysis of slice images and 3D rendered volumes can be used to better characterise a xenolith as a gt or gt-sp peridotite.

Variation of garnet content seen in the 3D volumes is due to clustering of garnet grains in the sample and since the garnets are general ellipsoidal in shape, the position of the slice image affects the volume of garnet observed. Based on point counting on a thin-section, sample VI 313 532 was characterised as a gt peridotite (Table 1) but based on the 3D volume slice images, it is clearly a gt-sp peridotite due to the presence of significant spinel volume in several gt-sp clusters. Modal mineralogy of sample VI 313 148 also shows a similar presence of a small volume of spinel in the CT scan.

### *Garnet-spinel cluster textures*

Micro-CT images of garnet-spinel clusters in peridotite xenoliths reveal the complex relationship between garnet and spinel (Figs. 4 - 9). Spinel is not just simply an inclusion in garnet but both minerals form complex structures. Slice images of the garnet grains have also revealed low density silicate inclusions. EMPA and BSE images of such inclusions in samples VI 313 116 and PA 18 (Fig. 3B) confirmed that they are olivine. Thus they record the solid-state reaction of pyroxene and spinel converting to garnet and olivine (equ 1).

The lineation seen in the gt-sp structures (Fig. 4) and the ellipsoidal shape of garnet grains and gt-sp clusters point to deformation which probably occurred while the rock was garnet-free. Fig. 10 shows that the highest mean aspect ratios are found in spinel-pyroxene clusters whilst the lowest are found in garnet peridotites. Garnet grains in the studied gt peridotites are somewhat ellipsoidal ( $AR = 1.2-1.4$ ) but their overall grain shape is much more spherical compared with the gt-sp structures ( $AR = 1.7-2.3$ ), which in turn are more similar to the shape of spinel-pyroxene clusters in mantle xenoliths from Lanzarote and the Massif Central (Bhanot et al., 2017). A micro-CT study of a garnet peridotite from Kaapvaal craton (not included in this study) shows an average garnet AR of 1.3, remarkably similar to those in spinel-free garnet peridotites in this study. Thus we conclude that the garnet growth occurred after deformation. This may also account for the clustered nature observed in the garnets.

The mineral compositions of the garnet-free peridotites are not systematically different from those of the garnet peridotites and, therefore, the difference in mineral assemblage must depend on the difference in physical conditions under which these peridotites recrystallized (Kushiro and Yoder, 1966). The boundary between the spinel- and garnet-lherzolite mineral facies is strongly curved between 1300°C and 1450°C; below 1200°C it lies almost parallel to the temperature axis on a T-P diagram (O'Hara et al., 1971). Experimental studies of the spinel to garnet transition show that it occurs at ~ 1.6 GPa at 1000°C in the CMAS (CaO-MgO-Al<sub>2</sub>O<sub>3</sub>-SiO<sub>2</sub>) system (Jenkins & Newton, 1979; Ionov et al., 1999; Klemme and O'Neill, 2000). However, the experiments of Robinson and Wood (1998) demonstrated that the minimum pressure at which garnet is stable on the anhydrous solidus of fertile peridotite is 2.8 GPa, corresponding to a depth of about 85 km and the spinel to garnet transition, which is 0.1–0.2 GPa wide, deepens as melt is extracted from the solid residue and solidus temperatures increase. Perkins and Anthony (1999) used bulk rock compositions to calculate equilibrium phase diagrams to calculate the conditions in which mineral assemblages are stable in the upper mantle. This approach requires consideration of the 7-component system SiO<sub>2</sub> – Al<sub>2</sub>O<sub>3</sub> – Cr<sub>2</sub>O<sub>3</sub> – FeO – MgO – CaO – Na<sub>2</sub>O, internally consistent thermodynamic data for end-members, and reliable mixing models for all mineral solutions. They showed that a specific mineral assemblage is stable over a range of P–T conditions and that the compositions of the individual minerals vary with changing P–T conditions, with the ol + cpx + opx + sp + gt five-phase assemblages having a very restricted stability field, i.e. ~0.5 kbar at 1100 °C.

The pressure interval where garnet and spinel coexist in the peridotite mantle beneath Vitim appears to be rather narrow (Ionov et al., 1993), when uncertainties of the geobarometry (Brey & Kohler, 1990) are considered. The garnet-spinel peridotites yield pressure estimates ranging from 1.6 to 1.95 GPa (980°C < T < 1045°C). This indicates a 'garnet-in' pressure of 1.6–1.7 GPa and a 'spinel-out' limit (for fertile peridotites) of ~2.0 GPa for Vitim xenoliths. Figure 11 is a pressure-temperature graph of equilibrium temperatures and pressures for gt and gt-sp peridotites from Vitim and Pali-Aike. The graph shows a distinction between phase assemblages where gt peridotites from Vitim plot in the high pressure (garnet) stability field whilst gt-sp peridotites plot in the relatively cooler and lower pressure region. Garnet-spinel peridotites from Pali-Aike plot at a higher pressure than those from Vitim.

Mantle xenoliths record the fact that different continental settings display mineralogical variations in relation to the age of the overlying crust; older sub-continental lithospheric mantle shows an increasing level of depletion indicated by low values of CaO and Al<sub>2</sub>O<sub>3</sub> in bulk rocks. Thus, Archean lithospheric mantle has a high Mg# (generally 93–95) coupled with low CaO and Al<sub>2</sub>O<sub>3</sub> contents. In contrast Proterozoic

and Phanerozoic sub-continental lithospheric mantle shows intermediate Mg# values and higher CaO and Al<sub>2</sub>O<sub>3</sub> bulk rock compositions. Depletion trends in mantle xenoliths thus record the mean level of depletion in the sub-continental lithospheric mantle from the Archean to the Phanerozoic (Artemieva, 2011). In mantle-derived garnet peridotite xenoliths, the Cr<sub>2</sub>O<sub>3</sub> content of garnet is correlated with generally accepted measures of depletion in basaltic components and high-Cr garnets are found in refractory rocks with high Mg#, low CaO and Al<sub>2</sub>O<sub>3</sub>, whereas low-Cr garnets are found in more fertile peridotites (Griffin et al., 1999). Cr<sub>2</sub>O<sub>3</sub> content of garnets from Vitim and Pali Aike are low, with a mean Cr# of 20 for Vitim and 28 for Pali Aike, whereas cratonic garnet Cr#s are generally ~65. CaO content in garnets from Vitim and Pali Aike range between 4.8-5.1 wt% and are thus distinct from the Cr- and Ca-rich garnets found in Kaapvaal-type (cratonic) peridotites.

In Fig. 3a, Vitim and Pali Aike peridotites plot within the lower part of the mantle array whilst cratonic peridotites occupy the more depleted (higher Cr# and Mg#) part of the array. Comparison of gt Mg# and Cr# (Fig. 3b) reveals a distinct difference between the more depleted cratonic garnets and the low-Cr garnets of the younger Pali Aike and Vitim. Based on modal cpx content and the mantle array diagram, the Pali Aike mantle is more depleted than the lithospheric mantle of Vitim.

Estimated equilibration temperatures and pressures for Vitim and Pali Aike were calculated using the Ca-opx thermometer of Brey and Köhler (1990) and the barometer of Nickel and Green (1985) and presented in the PT diagram in Figure 12, with additional data for Vitim from the study by Ionov et al (2005) and for Pali Aike from Wang et al (2008). Garnet spinel peridotites from both Pali Aike and Vitim occupy a region close to the oceanic geotherm (65 mW/m<sup>2</sup>) and show a narrow range of pressure and temperature, i.e. 18.4-23.2 kbar and 965-1121 °C. Cratonic peridotites from Kaapvaal (Simon et al., 2003) plot at greater depth (~ 125 km), display a wider range in temperature and pressure in comparison to both Vitim and Pali Aike, and plot close to the continental geotherm estimated at 40 mW/m<sup>2</sup>. Ionov et al (2005) stated that, assuming that temperature gradually increases with depth, the relative positions of the rock types in the lithospheric cross-section beneath Vitim can be inferred. Garnet–spinel peridotites coexist with spinel peridotites in the depth range ~60–70 km (18–21 kbar). Spinel peridotites, garnet–spinel and garnet peridotites occur together in the depth range ~70–75 km (21–22 kbar). Above 22 kbar garnet peridotite begins to dominate.

Garnet, garnet–spinel and spinel peridotites can coexist at pressures of 18–22 kbar because of differences in their bulk major element compositions, since the spinel–garnet phase transition takes place at greater depths in more refractory rocks (Ionov et al., 2005). Robinson and Wood (1998) also

pointed out that the spinel to garnet transition deepens as melt is extracted from the solid residue and solidus temperatures increase. This is probably why Pali Aike gt-sp peridotite samples plot with higher pressures than those from Vitim (Fig. 11).

The 3D volume of sample PA 31 from Pali-Aike displays a halo which surrounds spinel but not garnet. The halo is a phase denser than the silicate phase but significantly less dense than spinel and less dense than garnet. The halos are not isolated but appear to connect to channels and provide textural evidence of metasomatic reactions affecting the mantle. This phase is probably clinopyroxene.

Textures of single spinel-pyroxene complex structures in spinel peridotites from Lanzarote and Massif Central were investigated by Bhanot et al. (2017). Sizes of these structures range from 4 to 12 mm in the longest dimension. Their AR values range from 2.0 to 2.9. Their ellipsoid shape is attributed to flattening of originally spherical structures formed by replacement of large, originally equant, garnets with a spinel-pyroxene cluster (Bhanot et al., 2017). Gt-sp structures from Vitim and Pali-Aike display a similar ellipsoidal shape. Garnet grains in garnet peridotites from Vitim and Pali-Aike (PA18 and VI313116, Figs. 7 and 9B) also show ellipsoidal shapes but with a lower AR. The ellipsoidal shape of the gt-sp structures reflect the shape and size of the original deformed spinel-pyroxene clusters, whereas the newly grown garnets have a more spherical shape.

Garnets in micro-CT images of gt-spinel peridotites are visualized as separate grains with no evidence of chemical zoning relating to the kelyphite rim and its formation. Garnet and the associated complex spinel structure are very similar to spinel textures observed in spinel peridotite xenoliths from Massif Central and Lanzarote (Bhanot et al., 2017), albeit the spinel structures in PA and VI are less vermicular. Thus, they are considered to be relics of the original more vermicular spinel complex in a spinel-pyroxene cluster. Based on this observation, it is likely that the textures are related and thus act as examples of the garnet + olivine reaction with garnet ( $\pm$  ol inclusions) and spinel-pyroxene clusters are examples of the reversible sub-solidus reaction ( $\text{sp} + \text{opx} + \text{cpx} \leftrightarrow \text{ol} + \text{gt}$ ) going to completion, whereas the gt-sp textures seen in this study represent the transition stage of that reaction.

In addition, the size and texture of the spinel is relative to the degree of completion of the reaction, with less complex vermicular spinel textures representing the reaction near to completion (along with ol inclusions) relative to the more complex and more substantial spinel volume of the gt-sp cluster (PA 16). 3D rendered images of garnet grains show no concentric pattern, garnet appears as a single crystal with no evidence of distinct chemical zoning. The upper mantle beneath both Vitim and Pali-Aike has been



subjected to cooling and Ionov (2004) and Stern et al (1999) have proposed cooling of the lithosphere as the driving force for the development of gt and gt-sp peridotite textures. The 3D rendered volumes of both gt peridotites and gt-sp peridotites reveal that there is no interaction between the kelyphite rim and conversion of the original spinel-pyroxene cluster to garnet. Therefore, this process of kelyphite rim reaction forms no part of the gt-sp cluster formation process.

## *Conclusions*

CT scanning of garnet-spinel and garnet peridotite xenoliths from Vitim (Russia) and Pali-Aike (Patagonia) provides accurate representations of the textures of the constituent garnets and spinels. The complex textures shown in the 3D volumes reveal the tectonic histories of the upper mantle beneath the two localities. Garnets containing olivine inclusions and complex garnet-spinel structures are considered to be the products of the reaction between pyroxene and spinel ( $sp + opx + cpx \leftrightarrow ol + gt$ ). We have interpreted the textures to be evidence of a multi-stage process affecting the upper mantle. This process involves several stages. Firstly, the original garnet-bearing mantle was decompressed due to lithospheric thinning and followed the reverse reaction in equ 1 such that the garnet (and olivine) was transformed into spinel-pyroxene clusters. These clusters then experienced a period of deformation which changed their shapes to ellipsoids with aspect ratios of 2.0-2.9, similar to those of spinel-pyroxene clusters in other mantle xenoliths. We interpret the lineation of garnet-spinel clusters seen in sample PA 10 as deformation formed during the garnet-free phase and retained as the garnets grew. The final stage involves cooling and/or thickening of the lithosphere (Fig. 13) which transformed the spinel-pyroxene clusters back to garnet and olivine. Garnet-spinel clusters are interpreted to represent the incomplete conversion of a spinel-pyroxene cluster to garnet + olivine. Following conversion of spinel to garnet, garnet-spinel peridotites experienced metasomatic reactions as seen in the halo textures in sample PA 31. Finally, garnets were mantled with kelyphite rims due to increased heating prior to exhumation. We predict that the gt-sp cluster textures seen in Vitim and Pali-Aike gt-sp peridotites will form in regions which have experienced lithospheric thinning followed by isobaric cooling of the lithosphere.

## *Acknowledgments*

We thank Dimitri Ionov and Theo Ntaflos for providing samples from Vitim; the NHM (London) is thanked for providing samples from Pali-Aike, deposited by Pamela Kempton. We are also grateful to the X-ray CT scan facility at the Natural History Museum for CT data collection and help and advice provided in data processing. We thank Andy Beard for thin-section preparation and help and advice he provided with microprobe analysis. Krishan Bhanot would like to take this opportunity to thank Michael Hippler and Matthew Clarke at Rigaku Europe SE for financing his PhD project. We also thank the two anonymous reviewers and the editor Alan Woodland for their helpful comments.

## *References*

- Artemieva, I., 2011. Lithosphere: an interdisciplinary approach. Cambridge University Press.
- Bhanot, K.K., Downes, H., Petrone, C.M. and Humphreys-Williams, E., 2017. Textures in spinel peridotite mantle xenoliths using micro-CT scanning: Examples from Canary Islands and France. *Lithos*, 276, 90-102.
- Boyd, F.R., Pokhilenko, N.P., Pearson, D.G., Mertzman, S.A., Sobolev, N.V. and Finger, L.W., 1997. Composition of the Siberian cratonic mantle: evidence from Udachnaya peridotite xenoliths. *Contributions to Mineralogy and Petrology*, 128(2-3), 228-246.
- Brey, G.P. and Köhler, T., 1990. Geothermobarometry in four-phase lherzolites II. New thermobarometers, and practical assessment of existing thermobarometers. *Journal of Petrology*, 31(6), 1353-1378.
- Cao, R.L. and Zhu, S.H., 1987. Mantle xenoliths and alkali-rich host rocks in eastern China. *Mantle xenoliths* (Ed P H Nixon), pp.168-180.
- Carlson W D, T. Rowe T, Ketcham R A, M. W. Colbert M W 2003. Applications of high-resolution X-ray computed tomography in petrology, meteoritics and palaeontology. *Geological Society London, Special Publications* 215, 7-22
- Carswell, D.A., Clarke, D.B. and Mitchell, R.H., 1979. The petrology and geochemistry of ultramafic nodules from Pipe 200, northern Lesotho. *The Mantle Sample: Inclusion in Kimberlites and Other Volcanics*, 16, 127-144.
- Douglas, B.J., Saul, S.L. and Stern, C.R., 1987. Rheology of the upper mantle beneath southernmost South America inferred from peridotite xenoliths. *The Journal of Geology*, 95(2), 241-253.
- Gibson, S.A., McMahon, S.C., Day, J.A. and Dawson, J.B., 2013. Highly refractory lithospheric mantle beneath the Tanzanian craton: evidence from Lashaine pre-metasomatic garnet-bearing peridotites. *Journal of Petrology*, 54(8), 1503-1546.
- Godard, G. and Martin, S., 2000. Petrogenesis of kelyphites in garnet peridotites: a case study from the Ulten zone, Italian Alps. *Journal of Geodynamics*, 30(1-2), 117-145.

512 Green, D.H. and Ringwood, A.E., 1967. The stability fields of aluminous pyroxene peridotite and garnet  
513 peridotite and their relevance in upper mantle structure. *Earth and Planetary Science Letters*, 3, 151-  
514 160.

515 Grégoire, M., Bell, D.R. and Le Roex, A.P., 2003. Garnet lherzolites from the Kaapvaal Craton (South  
516 Africa): trace element evidence for a metasomatic history. *Journal of Petrology*, 44(4), 629-657.

517 Ionov, D., 2002. Mantle structure and rifting processes in the Baikal–Mongolia region: geophysical data  
518 and evidence from xenoliths in volcanic rocks. *Tectonophysics*, 351(1-2), 41-60.

519 Ionov, D., 2004. Chemical variations in peridotite xenoliths from Vitim, Siberia: inferences for REE and Hf  
520 behaviour in the garnet-facies upper mantle. *Journal of Petrology*, 45(2), 343-367.

521 Ionov, D.A. and Hofmann, A.W., 2007. Depth of formation of subcontinental off-craton peridotites. *Earth  
522 and Planetary Science Letters*, 261(3), 620-634.

523 Ionov, D.A., Ashchepkov, I. and Jagoutz, E., 2005. The provenance of fertile off-craton lithospheric  
524 mantle: Sr–Nd isotope and chemical composition of garnet and spinel peridotite xenoliths from Vitim,  
525 Siberia. *Chemical Geology*, 217(1-2), 41-75.

526 Ionov, D.A., Ashchepkov, I.V., Stosch, H.G., Witt-Eickschen, G. and Seck, H.A., 1993. Garnet peridotite  
527 xenoliths from the Vitim volcanic field, Baikal region: the nature of the garnet-spinel peridotite  
528 transition zone in the continental mantle. *Journal of Petrology*, 34(6), 1141-1175.

529 Ionov, D.A., Doucet, L.S. and Ashchepkov, I.V., 2010. Composition of the lithospheric mantle in the  
530 Siberian craton: new constraints from fresh peridotites in the Udachnaya-East kimberlite. *Journal of  
531 Petrology*, 51(11), 2177-2210.

532 Jenkins, D.M. and Newton, R.C., 1979. Experimental determination of the spinel peridotite to garnet  
533 peridotite inversion at 900 C and 1,000 C in the system CaO–MgO–Al<sub>2</sub>O<sub>3</sub>–SiO<sub>2</sub>, and at 900 °C with natural  
534 garnet and olivine. *Contributions to Mineralogy and Petrology*, 68(4), 407-419.

535 Kempton, P.D., Lopez-Escobar, L., Hawkesworth, C.J., Pearson, D.G., Wright, D.W. and Ware, A.J., 1999.  
536 Spinel ± garnet lherzolite xenoliths from Pali Aike: Part 1. Petrography, mineral chemistry and  
537 geothermobarometry. JB Dawson volume. *Proceedings of VIIth International Kimberlite Conference*, pp.  
538 403-414.

539 Ketcham R A and Carlson W D. 2001. Acquisition, optimization and interpretation of X-ray computed  
540 tomographic imagery: applications to the geosciences. *Computers & Geosciences* 27, 381–400.

541 Klemme, S. and O'Neill, H.S., 2000. The near-solidus transition from garnet lherzolite to spinel lherzolite.  
542 *Contributions to Mineralogy and Petrology*, 138(3), 237-248.

543 Kruth J P, M. Bartscher M. Carmignato Schmitt R, De Chiffre L, Weckenmann A. 2011. Computed  
544 tomography for dimensional metrology. *CIRP Annals - Manufacturing Technology* 60, 821–842

545 Kushiro, I. and Yoder Jr, H.S., 1966. Anorthite-forsterite and anorthite-enstatite reactions and their  
546 bearing on the basalt-eclogite transformation. *Journal of Petrology*, 7(3), 337-362.

547 Mercier, J.C. and Nicolas, A., 1975. Textures and fabrics of upper-mantle peridotites as illustrated by  
548 xenoliths from basalts. *Journal of Petrology*, 16(1), 454-487.

549 Murav'yeva, N.S., Polyakov, A.I. and Senin, V.G., 1985. Physicochemical conditions and mechanism of  
550 formation of garnet-spinel lherzolite from the Vitim Plateau, Baikal rift zone. *Doklady Akademii Nauk*  
551 SSSR, 283, 1458-1462.

552 Nickel, K.G. and Green, D.H., 1985. Empirical geothermobarometry for garnet peridotites and  
553 implications for the nature of the lithosphere, kimberlites and diamonds. *Earth and Planetary Science*  
554 *Letters*, 73(1), 158-170.

555 O'Hara, M.J., Richardson, S.W. and Wilson, G., 1971. Garnet-peridotite stability and occurrence in crust  
556 and mantle. *Contributions to Mineralogy and Petrology*, 32(1), 48-68.

557 Perkins, D. and Anthony, E.Y., 2011. The evolution of spinel lherzolite xenoliths and the nature of the  
558 mantle at Kilbourne Hole, New Mexico. *Contributions to Mineralogy and Petrology*, 162(6), 1139-1157.

559 Petit, C., Koulakov, I. and Deverchère, J., 1998. Velocity structure around the Baikal rift zone from  
560 teleseismic and local earthquake traveltimes and geodynamic implications. *Tectonophysics*, 296(1-2),  
561 125-144.

562 Ramakrishna K, Muralidhar, and P Munshi K. 2006. Beam-hardening in simulated X-ray tomography. *NDT*  
563 *& E International*, 39, Pp 449–457.

564 Reid, A.M., Donaldson, C.H., Brown, R.W., Ridley, W.I. and Dawson, J.B., 1975. Mineral chemistry of  
565 peridotite xenoliths from the Lashaine volcano, Tanzania. In *Physics and Chemistry of the Earth*, 525-  
566 543. Pergamon.

567 Robinson, J.A.C. and Wood, B.J., 1998. The depth of the spinel to garnet transition at the peridotite  
568 solidus. *Earth and Planetary Science Letters*, 164(1-2), 277-284.

569 Simon, N.S., Irvine, G.J., Davies, G.R., Pearson, D.G. and Carlson, R.W., 2003. The origin of garnet and  
570 clinopyroxene in “depleted” Kaapvaal peridotites. *Lithos*, 71(2-4), 289-322.

571 Skewes, M.A. and Stern, C.R., 1979. Petrology and geochemistry of alkali basalts and ultramafic  
572 inclusions from the Palei-Aike volcanic field in southern Chile and the origin of the Patagonian plateau  
573 lavas. *Journal of Volcanology and Geothermal Research*, 6(1-2), 3-25.

574 Smith, D., 1977. The origin and interpretation of spinel-pyroxene clusters in peridotite. *The Journal of*  
575 *Geology*, 85(4), 476-482.

576 Stern, C.R., Kilian, R., Olker, B., Hauri, E.H. and Kyser, T.K., 1999. Evidence from mantle xenoliths for  
577 relatively thin (< 100 km) continental lithosphere below the Phanerozoic crust of southernmost South  
578 America. In: *Developments in Geotectonics*, 24, 217-235.

579 Wang, J., Hattori, K.H., Li, J. and Stern, C.R., 2008. Oxidation state of Paleozoic subcontinental  
580 lithospheric mantle below the Pali Aike volcanic field in southernmost Patagonia. *Lithos*, 105(1-2), 98-  
581 110.

582

583 Figure Captions

584

585 Fig. 1a. Garnet peridotite thin-section PPL image (VI 313 532). Garnet grains are mantled by  
586 kelyphite rims. Scalebar is 5mm. Fig. 1b. Garnet-spinel peridotite thin-section PPL image (PA  
587 16). Garnet-spinel clusters display complex vermicular structures and are mantled by a  
588 kelyphite rim. Scalebar is 5mm.

589 Fig. 2a. BSE image of gt-sp cluster and kelyphite rim (PA 16). Fig. 2b. BSE image of garnet with ol  
590 inclusion and kelyphite rim in a garnet peridotite (PA 18). Scale bar 1mm.

591 Fig. 3a. OSMA diagram for sp peridotites and gt-sp peridotites from Vitim, Pali-Aike and cratonic  
592 peridotites. Data taken from this study and Ionov et al., 2005; Ionov et al., 2010; Gibson et al.,  
593 2013 and Simon et al., 2003. Cratonic peridotites are shown as solid diamond, Pali Aike sp  
594 harzburgites as solid circles, Vitim sp Iherzolites as open circles, Pali Aike gt-sp peridotites as  
595 solid squares and Vitim gt-sp peridotites as open squares. Fig. 3b. Cr# vs mg# in garnets in Vitim  
596 (open circle) and Pali Aike (solid circle) xenoliths compared with cratonic peridotites (solid  
597 diamond). Cratonic peridotite data taken from Carswell et al., 1979; Grégoire et al., 2003; Ionov  
598 et al., 2010; Gibson et al., 2013; Reid et al., 1975 and Simon et al., 2003.

599 Fig. 3. 3D rendered image of gt-sp cluster in sample PA 10. Garnet coloured yellow, spinel  
600 shown as red. Scalebar is 10mm.

601 Fig 4. Series of 3D rendered images of gt-sp cluster (PA 16) with increasing garnet transparency.  
602 Garnet coloured yellow, spinel shown as red. Scale bar is 3.585 mm.

603 Fig. 5. 3D rendered image of gt-sp cluster (PA 13). Garnet coloured yellow, spinel shown as red.  
604 Scalebar is 4.033 mm.

605 Fig. 6. 3D rendered image of gt-sp cluster (PA 18). Garnet coloured yellow, spinel shown as red.  
606 Scale bar is 7.58 mm.

607 Fig. 7a. 3D rendered image of gt-sp cluster (PA 31). Garnet coloured yellow, spinel shown as  
608 red. Scale bar is 12.28mm. Fig 8b. 3D rendered image of gt-sp cluster (PA 31) with a  
609 metasomatic halo encasing gt-sp clusters. Garnet coloured yellow, spinel shown as red and  
610 metasomatic halo shown as green. Scale bar is 5mm.

611 Fig. 9a. 3D rendered image of garnet grains in gt peridotite VI 313 1270. Garnet coloured  
612 yellow. Scale bar is 10 mm. Fig. 9b. 3D rendered image of gt-sp cluster (VI 313 532), garnet  
613 coloured yellow and spinel red. Scale bar is 10 mm.

614 Fig. 10. Box and whisker plot of aspect ratios (AR) for spinel peridotites from Massif Central  
615 (France), Lanzarote (Spain) and Calatrava (Spain) containing spinel-pyroxene clusters, and for gt  
616 peridotites and gt-sp peridotites from Vitim (Russia) and Pali Aike. Aspect ratios for garnet in gt  
617 peridotites from Kaapvaal craton included for comparison. Mean ARs are shown as a solid black  
618 circle.

619 Fig. 11. Graph of equilibrium temperatures and pressures for gt and gt-sp peridotites from  
620 Vitim and Pali-Aike. Data from Ionov et al. (1993), Wang et al. (2008). Representative gt-sp

621 transition from Green and Ringwood (1967). Vitim gt lherzolites, solid square, Vitim gt-sp  
622 lherzolites, open square, Pali Aike gt-sp lherzolites, open circle. Temperatures and pressures  
623 calculated using Brey and Köhler (1990) Ca-in-Opx thermometer.

624 Fig. 12. P-T diagram comparing mantle peridotites from Pali-Aike (open square) and Vitim (open  
625 circle), sp peridotites (Vitim, cross) with cratonic mantle xenoliths (open diamonds). Data from  
626 Simon et al. (2003); Ionov et al. (2005) and Wang et al. (2008). Temperatures and pressures  
627 calculated using Brey and Köhler (1990) Ca-in-Opx thermometer, and Nickel and Green (1985)  
628 Al-in-Opx barometer. Gt-sp transition from Green and Ringwood (1967) is representative only,  
629 as this varies in depth according to the composition of the mantle.

630 Figure 13. Mantle facies diagram showing schematic transition of sp peridotite to gt peridotite  
631 stability field by a decrease in pressure (1) followed by isobaric cooling (2) and exhumation (3).  
632 Adapted from Perkins and Anthony (2011).

633

# Micro-CT investigation of garnet-spinel clusters in mantle peridotite xenoliths

K.K. Bhanot <sup>a, b</sup>, H. Downes <sup>a, b</sup>, C.M. Petrone <sup>b</sup>, E. Humphreys-Williams <sup>c</sup>, B. Clark <sup>c</sup>

<sup>a</sup> Department of Earth and Planetary Sciences, Birkbeck University of London, Malet Street, London WC1E 7HX, UK

<sup>b</sup> Department of Earth Sciences, Natural History Museum, Cromwell Road, London SW7 5BD, UK

<sup>c</sup> Imaging and Analysis Centre, Natural History Museum, Cromwell Road, London SW7 5BD, UK

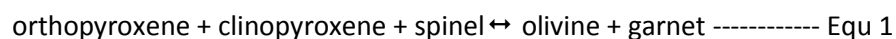
## Abstract

We have investigated the origin of garnet in garnet-spinel peridotite mantle xenoliths from two well-known localities, Pali-Aike (Patagonia) and Vitim (Siberia). We used micro-CT scanning to **examine** the textures of garnet-spinel clusters and the relationship between garnet and spinel. CT scanning yields different mineral modes in terms of spinel and garnet than **observed** in thin-section, because distribution of these phases is inhomogeneous, and a larger volume is visible in **a CT scan than in a thin-section**. We conclude that garnet formed after spinel in both localities, but the xenoliths record a complex tectonic history, in which the original garnets in garnet peridotites were transformed to spinel-pyroxene clusters in spinel peridotites, via lithospheric thinning. This stage was followed by deformation of the spinel peridotites, producing a **lineation**. A final stage of **isobaric** cooling caused garnet to re-grow around the spinel clusters. **Aspect ratios of garnets differ from those of garnet-spinel clusters; the latter are more similar to those of spinel pyroxene clusters**. Kelyphite is a secondary feature resulting from **heating and rapid decompression** during entrainment in the host alkali basaltic lavas and has no relationship with the formation of the garnet-spinel clusters.

Keywords: garnet-spinel peridotite; mantle xenolith; Vitim; Patagonia, **CT scanning**

## Introduction

Garnet-bearing peridotite mantle xenoliths are rare in off-craton alkali basaltic areas and are only reported from a few alkali basaltic provinces such as Patagonia (Skewes & Stern, 1979; Kempton et al, 1999), Siberia (Murav'yeva et al., 1987) and China (Cao & Zhu, 1987; Ionov, 2004). In studies of spinel-garnet peridotite xenoliths, Ionov et al. (1993), Ionov (2004) and Stern et al. (1999) concluded that the garnets were formed at the expense of spinel and pyroxenes in a sub-solidus reaction. This sub-solidus transition from the spinel stability field to the garnet stability field is caused by either a decrease in temperature or an increase in pressure, and is represented by the reversible equation (Smith, 1977):



This study will test the hypothesis that garnets formed from spinel and pyroxenes in suites of garnet-spinel peridotite xenoliths by using micro-CT scanning to determine their three-dimensional textures and the relationships between garnet and spinel. Micro-CT 3D volumes provide accurate and high-resolution representations of both garnet and spinel phases in peridotites. Analysis of the 3D volumes will allow comparison of garnet-spinel textures in samples from the two localities, including their aspect ratios. We will compare these with 3D textures of spinel-pyroxene clusters in spinel peridotite mantle xenoliths (Bhanot et al., 2017) which provide textural evidence of the reverse of the reaction shown in Equ 1.

## Sample localities

Our samples are from two well-known off-craton continental mantle xenolith localities: Pali-Aike (PA) in South America, and Vitim (VI) in eastern Russia. The Pali-Aike volcanic field forms part of the Patagonian plateau lavas and is  $\leq 4$  Ma in age. The western margin of South America is a convergent plate boundary between the South American, Nazca and Antarctic plates (Skewes and Stern 1979). The Pali-Aike host basalts are alkali-olivine basalts generated by partial melting of the mantle in response to tectonic changes of the South American, Nazca and Antarctic plate triple junction.

The Vitim plateau is composed of Cenozoic alkali basaltic lava flows and pyroclastic deposits, located  $\sim 250$  km east of Lake Baikal. Tectonic and geophysical studies (e.g. Petit et al., 1998) have found no evidence for large-scale lithospheric thinning beneath the Vitim plateau (Ionov, 2002). Because the Vitim



plateau is clearly distinct from the Baikal rift in terms of its relief and tectonic setting, it may be more appropriate to consider it as part of the broad diffuse area of Cenozoic alkali basaltic volcanism between the Siberian and North China cratons (Ionov 2004).

Textures and petrology of mantle xenoliths from Pali-Aike have been previously studied by Skewes and Stern (1979), Douglas et al. (1987), Stern et al. (1999), Kempton et al. (1999) and Wang et al. (2008). They are high-temperature (>970°C) peridotites, mostly protogranular garnet-spinel harzburgites and garnet lherzolites. Low temperature spinel peridotites were not studied. Previous studies of textures and petrology of Vitim mantle xenoliths include those of Ionov et al. (1993), Ionov (2004), Ionov et al. (2005) and Ionov and Hoffman (2007). Xenoliths from Vitim are protogranular garnet-spinel or garnet lherzolites.

### 3. Methodology

Thin-section preparation and electron microprobe analysis (EMPA) were performed at Birkbeck, University of London. The modal mineralogy was calculated by point-counting from scanned images of thin-sections. BSE images, elemental mapping and major element mineral analyses were obtained using a Jeol JXA8100 Superprobe with an Oxford Instruments Aztec energy dispersive system (EDS) at Birkbeck. EDS analysis was carried out using an accelerating voltage of 15 kV, a current of 10 nA and a beam diameter of 1 µm. EDS analyses were calibrated against standards of natural silicates, oxides and Specpure® metals with the data corrected using a ZAF (atomic number, absorption and fluorescence) correction program.

Cylindrical cores of 25 mm diameter and approximately 25 mm length were drilled from the peridotite xenoliths for CT scanning. The shape and size of the cores were chosen to ensure equal absorption and penetration of the X-ray beam, thus reducing artefacts in the final 3D rendered CT volume. One sample (VI 313-1270) was analysed without being cored; this made little difference to the processed CT results but provided a larger volume for analysis.

Computed tomography (CT) acquires multiple sets of images of the sample over 360°. The 2D images are processed (reconstructed) to yield the raw dataset. During reconstruction, raw intensity data are converted to CT values which map linearly to the effective attenuation coefficient of the material in each voxel (Ketcham and Carlson 2001). A single tomographic slice is a cross-sectional layer of the sample and is composed of smaller divisions known as volume elements or “voxels”. In a digital image, voxel

dimensions are related to the size of a pixel and to the sum of attenuation with respect to the X-ray path. Resolution of the measurement and reconstruction is influenced by pixel size, number of pixels within each grey value profile, number of pixels or slices in the Y direction and number of angular positions (Kruth et al., 2011).

The principal configuration for CT data acquisition involves a stationary X-ray (polychromatic) source, a rotational sample stage and an X-Ray detector. The specimen is mounted on the rotating stage between the X-ray source and detector. The geometry of the specimen and X-ray source dictates the CT image resolution. By reducing the specimen-to-source distance along the magnification axis, a more magnified and better resolved image is captured at the detector, compared with a specimen at a greater distance from the X-ray source. However, higher magnification may cause blurring of the image when using a reflection target.

Since X-ray absorption is a measure of material density, its distribution within 3D images provides an insight into the internal structures and distribution of phases in a specimen. Phase analysis for 2D and 3D images is carried out by utilising the voxel intensity (grey-scale) histogram, which plots the frequency of voxels at a particular intensity and so permits the separation (segmentation) of an image into distinct phases. One major factor that must be considered when evaluating voxel intensity histograms taken from multiphase data is overlapping intensities of the different phases.

Carlson et al. (2003) reviewed the application of CT scanning in the Earth Sciences. Geological samples consist of multiple minerals of different densities and it is important to understand how such samples will react to exposure to the X-ray beam. Attenuation characteristics allow us to predict the possibility of differentiating between different minerals in CT images (Ketcham and Carlson, 2001). However, the attenuation curves for forsterite and enstatite are similar across the whole range of X-ray energies, which makes it very difficult to distinguish between these two minerals. Clinopyroxene has a higher attenuation factor at low energies (50 keV) because of the high atomic number of Ca, and so it can be distinguished in CT images. Garnet (pyrope) has a higher attenuation coefficient across the whole range of energies compared with the silicate minerals and is distinguishable in slice images. Spinel, with high density and a high linear attenuation coefficient across the whole range of energies, is easily distinguishable from the silicates. Thus, during segmentation, the garnet, spinel and silicate phases can be viewed in isolation, as can Ca-rich minerals such as clinopyroxene. With the spinel and silicate phases isolated, the 3D rendered visualisations show the grain size, shape and distribution of garnet and spinel within each rock core.

Micro-CT scans were collected at the NHM on the Metris X-Tek HMX ST 225 scanner coupled with a 4-megapixel Perkin Elmer XRD 1621 AN3 HS detector panel. The power setting for data collection for a polychromatic X-ray beam (cone beam projection) with a tungsten target (reflection target) and Cu filter (thickness 1.0 mm) was 190 kV and 210  $\mu$ A. Resolution of the 3D rendered volumes ranged from 13 to 19  $\mu$ m. The rock cores were mounted inside the X-ray enclosure and housed on a translation stage. The distance of the sample to source was set to ensure maximum magnification without introducing blurred edges. The cores were scanned with 3142 projections and an exposure time of 1000 ms.

CT scans can be affected by various artifacts which can compromise the quality of the 3D rendered volume. Beam hardening is an artefact in which the edges of an image appear more intense compared to its centre (Ramakrishna et al. 2006). To minimise this effect, we tried both Cu and Al attenuation filters with varying thickness before the X-ray beam interacted with the sample, to reduce the low energy X-rays, and found that a Cu filter with a thickness of 1 mm provided the optimum conditions.

The Avizo software suite was used for 3D segmentation and volume rendering. The data sets were analysed, segmented and rendered, and four phases were identified, i.e. air, silicate minerals, garnet and spinel. Initial data sets of garnet peridotite cores yielded data highly susceptible to beam hardening. The result was that, although the spinel was easily segmented, the garnet phase could not be accurately segmented from the other silicate phases. The scan conditions were varied in order to optimise data collection. Different X-ray tube power settings and the sample-to-source distances were tested.

Although beam hardening could not be completely removed, the optimum machine conditions are as shown above. The effect of beam hardening poses a problem in segmenting similar material at the edge of the data set compared to its centre, because mean grey values for garnets at the edge appear higher than mean grey values at the centre of the 3D data set. To overcome this, the data set was cropped into a rectangular box and only the central portion was selected. A major disadvantage is that, since the large garnets are often clustered and unevenly distributed, whole garnets were often also cropped, thus reducing our ability to truly image the garnet texture. Two samples from Vitim suffered from this effect and were omitted from the data set.

Avizo has a “region-growing” utility (called a “magic wand”) in which different material can be manually selected in the individual slice images based on defined grey value range of voxels for all connected voxels, which can be assigned to that material automatically. Care must be taken that other materials are not selected and assigned incorrectly, since the attenuation coefficients for garnet are close to other silicates for samples from Vitim and Pali-Aike because of the low Cr<sub>2</sub>O<sub>3</sub> content (<2wt %) in the garnets.

Garnet and other silicate phases overlap in the 3D slice histogram and use of the region-growing can lead to errors in segmentation.

The “Volume Fraction” tool in Avizo was used to calculate the volume fraction for garnet and spinel in samples from Vitim and Pali Aike. The volume fraction tool works by comparing the number of voxels of a selected material with the total number of voxels of the sample. Volume fractions are listed in Table 1. The aspect ratio (AR) of garnets and garnet-spinel clusters were obtained from the raw 3D volume data by using ImageJ software to measure the longest and shortest axes. For comparison, the same methodology was applied to garnets in cratonic garnet peridotite xenoliths and to spinel-pyroxene clusters in xenoliths from Massif Central and Lanzarote (Bhanot et al., 2017). Videos and images of 3D volumes are available in the Supplementary data.

## Results

### Textural and modal analyses in thin-section

The modal mineralogy of the mantle xenoliths in thin-section (Table 1) shows that the samples include both garnet-spinel peridotites and garnet peridotites, but no pure spinel peridotites. All the xenoliths are coarse-grained and protogranular following the classification of Mercier and Nicolas (1975). Mineralogy consists of olivine (forsterite), orthopyroxene (enstatite), clinopyroxene (diopside),  $\pm$  spinel and garnet (pyrope). Garnet-spinel peridotites from Pali-Aike are largely harzburgites whilst those from Vitim are mostly lherzolites (Table 1). Garnet peridotites from Pali-Aike are also mostly harzburgites whereas those from Vitim are largely garnet lherzolites with one harzburgite. This suggests that samples from Pali Aike have experienced more depletion than those from Vitim. Figure 1 shows images of thin-sections of a gt lherzolite from Vitim and a gt-sp lherzolite from Pali-Aike. The samples from Vitim showed a surprising lack of spinel (Table 1).

BSE images of gt-sp peridotites and gt peridotites from both localities show coarse-grained anhedral garnets which vary in size (Fig. 2). They have irregular but generally circular grain shapes and often contain olivine inclusions. Garnets are often not randomly distributed but appear to be clustered. Spinel in gt-sp peridotites are associated with garnets and often occur as inclusions within garnets (Fig.

2a), where they form the central core surrounded by garnet. Spinel shapes vary from small blebs to large vermicular grains. The content of spinel in thin-sections of samples from Vitim is <1% whilst in those from Pali-Aike spinel content is <3% (Table 1). Garnets display no chemical zoning but are commonly mantled with a kelyphite rim (Fig. 2b) composed of garnet, cpx and spinel. Spinel and cpx grains in kelyphite rims in Vitim samples can be zoned. The contacts between garnet and spinel inclusions are also mantled with a kelyphite rim showing a similar texture to the rim surrounding the garnet.

#### *Garnet-spinel peridotites*

Garnets in garnet-spinel clusters from Vitim vary in size from <5 mm weakly elliptical to highly elliptical vermicular structures. In samples from Pali-Aike the garnet-spinel clusters are also highly elliptical, >4 mm in length and <3 mm in width, and display a vermicular texture. In thin-section, spinels vary from blebs with a mild vermicular texture inside the garnets to complex vermicular structures. Volume of spinel can vary from small individual blebs to larger complex structures forming a larger percentage of the garnet-spinel complex (PA 10).

#### *Garnet peridotites*

Garnet content in thin-sections of garnet peridotites ranges from 4 to 26% in xenoliths from Vitim and from 3 to 6% in Pali-Aike samples. Garnets in Vitim samples (Fig. 1) vary from ~2 mm rounded grains to highly elliptical vermicular grains >4 mm in length (e.g. VI 313 1278). Garnets from Pali-Aike are largely equant and approximately 2 mm in diameter (e.g. PA 18). Garnets from both locations often contain small rounded inclusions of olivine (Fig. 2b).

### Mineral chemistry

Microprobe analyses of samples from Pali-Aike (PA) and Vitim (VI) in this study (Supplementary files) are similar to previous studies from the two regions (Skewes and Stern, 1979; Stern et al., 1999; Ionov et al., 1993). Both gt-sp peridotites and gt peridotites have a similar mineral composition. Mg#s ( $Mg\# = \frac{Mg}{Mg + Fe} \times 100$ ) for olivine, orthopyroxene and clinopyroxene from the two localities are similar in the range of 88-90. Spinel Cr#s ( $Cr\# = \frac{Cr}{Cr + Al} \times 100$ ) are higher in PA samples (21–32) than in VI (19–20).  $Al_2O_3$  contents in spinel are 36-47 wt%,  $Cr_2O_3$  is 17-27 wt%, MgO is 16-20 wt% and FeO is 12-18 wt%.

Orthopyroxenes from both localities are enstatites with 3.5-4.4 wt%  $\text{Al}_2\text{O}_3$ . Clinopyroxenes are diopside containing 17-19 wt% CaO, 5-11 wt%  $\text{Al}_2\text{O}_3$  and <1.5 wt%  $\text{Cr}_2\text{O}_3$ . Garnets are pyrope with Mg#s 81-85. Their  $\text{Al}_2\text{O}_3$  content is 23 wt%,  $\text{Cr}_2\text{O}_3$  is 1.1 wt%, MgO is 20 wt%, CaO is 5 wt% and FeO is 8 wt%. Garnets in several samples from both localities contain olivine inclusions with Mg#s of 89-90, identical to olivines outside garnets. NiO content in both olivine inclusions inside garnets and outside garnets are also similar at <0.4 wt%.

Arai (1994) outlined how the values of Mg# in olivine and Cr# in spinel can constrain the origin of spinel peridotites. Spinel lherzolites and spinel harzburgites have limited ranges of  $\text{Mg\#}_{\text{olivine}}$  and  $\text{Cr\#}_{\text{spinel}}$  values, forming the olivine - spinel mantle array (OSMA). Since we have no xenoliths which are purely spinel-bearing, we have used EMPA analysis of spinel peridotites from Vitim (Ionov et al., 1995) and Pali Aike (Skewes and Stern, 1979; Wang et al., 2008) (Fig 3a). Comparing our data to previous results for spinel peridotites from the same locations, Vitim samples have higher spinel Cr#s than in spinel peridotites, but Pali Aike samples show the opposite. Ol Mg#s for VI and PA are 90 and 89, respectively. All analysed spinel Cr#s from VI and PA are much lower than those of cratonic spinel peridotite xenoliths (Fig. 3a).

Garnet compositions from Vitim and PA have Cr#s of 3.4-3.5 which are much lower than those of gt and gt-sp peridotites from Udachnaya (Ionov et al., 2010), Lashaine (Reid et al., 1975; Gibson et al., 2013) Kaapvaal (Carswell et al. (1979); Grégoire et al. (2003); Simon et al. (2003)) which vary from 11 to 33 (Fig 3b). Mg#s of VI garnets are lower than those of PA, again suggesting that the PA samples have experienced more depletion.

Kelyphite rims around garnets have an average thickness of 100  $\mu\text{m}$ , which is uniform in samples from both VI and PA. Kelyphite rims display a sharp contact with garnet cores. BSE images of reaction rims arounds garnets in this study show that the kelyphite symplectite microstructures, often associated with coronae mantling garnet peridotite (Godard and Martin, 2000), are largely absent in PA and VI samples. However, one sample does show a partial portion displaying a fibrous symplectite texture. Kelyphite rims from PA and VI are composed of cpx and spinel and a secondary garnet which is more Mg-rich (Mg# 85) but with lower  $\text{Al}_2\text{O}_3$  and CaO than the garnet cores. A third garnet exists in small regions in sharp in contact with the garnet core (PA 16). This garnet is more Ca-rich with 14 wt% CaO. Both Mg# (60) and Cr# (0.8) are considerably lower than the garnet core. Spinel and cpx in the kelyphite rims can be zoned (e.g. VI 313- 1278). The contact between garnet and spinel inclusions are also mantled with a kelyphite rim displaying a similar texture to the rim surrounding garnet. The presence zoning in grains in the kelyphite rim and the absence of the kelyphite texture from the cores implies that the kelyphite rim is a

secondary texture and is thus independent of the sub-solidus reaction shown in Equ 1. In fact, it is the reverse reaction ( $gt_1 + ol$  goes to  $sp + pyx + gt_2$ ) and is related to exhumation.

## Micro CT results

Modal abundances for garnet and spinel calculated from the 3D volume fraction and measured in thin-section by point counting show significant differences (Table 1). Garnet modal values from Vitim are generally higher in the micro-CT volume, but the reverse is true for samples from Pali Aike. In most cases, the spinel modal abundance is much lower in the 3D volume than in thin-section. However, in the cores of two of the Vitim xenoliths, very little garnet was found despite it being present in the thin-sections. This suggests that neither method accurately represents the actual modal abundances of these very coarse-grained rocks, but since the volume being analysed by CT-scanning is much greater than the area represented by a thin-section, the CT scans probably yield a more accurate result.

## Pali-Aike

In the Pali-Aike xenoliths, spinel is generally found in clusters with garnet, with a few exceptions in which spinels are found as individual isolated crystals. Micro-CT scans of garnet-spinel (gt-sp) clusters reveal a range of textures including (a) randomly orientated large elliptical (>2 mm) garnet grains, (b) large elliptical (>2 mm) garnet grains encasing small individual spinel blebs, (c) large (<4 mm) garnet grains encasing large complex spinel structures, (d) complex and highly elongate garnet-spinel clusters displaying a strong lineation. Distribution of garnets through the cores is often random but the garnets also occur as clusters with large volumes of the sample devoid of garnet. The individual spinel blebs form a small volume of the gt-sp cluster whereas the complex, highly vermicular spinel structures form a much higher volume of the gt-sp cluster.

The different samples from Pali-Aike show slightly different features. In PA 10, a garnet-spinel harzburgite (Fig. 4), the individual gt-sp structures vary from <10 mm in length and <2 mm in width to small gt-sp clusters <2 mm in the longest dimension. Their average AR is 2.3. Spinel forms much of the volume of these structures, whilst several spinel crystals have no associated garnet. Individual gt-sp structures often show a strong lineation (Fig. 4).

266 Garnet-spinel harzburgite sample PA 16 (Fig. 5) shows examples of the individual large complex gt-sp  
267 clusters displaying the ellipsoidal garnet shapes and vermicular spinel texture within the cluster. The gt-  
268 sp clusters are individual ellipsoidal structures which measure <4 mm in length and <2 mm in width,  
269 with a mean AR of 1.9. Garnet displays a vermicular texture and all spinel is associated with garnet.  
270 Spinel forms much of the volume of these structures. Spinel also forms complex and highly vermicular  
271 features enclosed within the garnet. The large complex spinel structure shows individual spinel branches  
272 which are in contact with adjacent branches, thus forming a single crystal of spinel.

273 Sample PA 13 (Fig. 6) is a good example where garnet grains are clustered but show no alignment. The  
274 3D rendered volume shows much of the sample is devoid of garnet and spinel. Garnets in PA 13 are  
275 large individual grains that measure <4 mm in length and <2 mm in width, with a mean AR of 1.9.  
276 Several garnets grains are clustered in the sample core with large volumes free of both spinel and  
277 garnet. Spinel forms a low volume compared to garnet and exists as small blebs <1 mm. All spinel is  
278 associated with garnet.

279 Garnets in garnet harzburgite sample PA 18 (Fig. 7) are large individual grains that measure between <4  
280 mm in length and <2 mm in width to <2 mm in diameter and are more spherical in shape (mean AR =  
281 1.4). Garnets are randomly distributed throughout the core but regions with a higher density of garnet  
282 are visible where individual garnet grains are clustered. Spinel forms a very low volume compared to  
283 garnet and exists as small blebs <1 mm only in several grains, with most of the garnet being spinel-free.  
284 Spinel is not limited to gt-sp clusters, but several small blebs are visible in the core in garnet-free  
285 regions.

286 Sample PA 31 (Fig. 8) is a gt-sp peridotite. Garnet grains are randomly distributed throughout the core  
287 and vary in shape from complex vermicular grains with no spinel to spherical <4 mm size gt-sp structures  
288 (mean AR = 2.2). Large ellipsoidal spinel blebs <4 mm in size with a strong vermicular texture are not  
289 associated with garnet but are also randomly distributed throughout the core. In PA 31, garnet-free  
290 spinel blebs are surrounded by a halo of high atomic number material which is less dense than both the  
291 garnet and spinel phases (Fig. 8b). There is enough density contrast of the halo for it to be resolved from  
292 the silicate phase and is interpreted as products of metasomatic reactions similar to metasomatic halos  
293 in spinel-pyroxene clusters from Lanzarote spinel harzburgite xenoliths (Bhanot et al., 2017). This  
294 metasomatism probably accounts for the high cpx content in PA 31 (Table 1).



## Vitim

Micro-CT scans of gt-sp clusters in samples from Vitim show large ellipsoidal (>2 mm) garnet grains encasing individual spinel blebs and large (<4 mm) garnet grains enveloping complex spinel structures with a strong vermicular texture. Distribution of garnets through the cores is random but the garnets are often clustered such that large volumes of the core are devoid of garnet, as in the Pali-Aike samples. Also, like samples from Pali-Aike, individual spinel blebs form a small volume of the gt-sp cluster whilst the complex, high vermicular spinel structures form a higher volume of the complex. The large complex spinel structures are ellipsoidal and individual spinel branches are in contact with adjacent branches, thus forming a single crystal of spinel.

Garnet lherzolite VI 313 1270 was the only sample that was CT-scanned without being cored and so it provided the largest imaged volume of any studied xenolith. It is also the only sample which did not contain any spinel in the 3D scan (Table 1). Fig. 9a shows that the garnets are large individual grains that measure between <4 mm in length and <2 mm in width to <2 mm in diameter and are more spherical (mean AR = 1.3). Garnets are randomly distributed throughout the core but regions with a higher density of garnet are visible where individual garnet grains are clustered.

Modal mineralogy based on thin-section analysis revealed sample VI 313 532 to be a gt lherzolite. However, analysis of the 3D volume revealed the presence of gt-sp clusters. Spinel forms a low volume compared to garnet and exists as blebs <5 mm and complex, vermicular structures with an ellipsoidal shape. Spinel is not limited to gt-sp clusters, but several small blebs (<1 mm) are also visible. Garnets in garnet-spinel peridotite VI 313 532 (Fig. 9b) are large individual ellipsoidal grains that measure <5 mm in length and <4 mm in width. Garnets are randomly and evenly distributed throughout the core. There is no spinel visible in the scan of the core of this sample, although some had been found in thin-section (Table 1).

Mean ARs for garnet in gt peridotites from Vitim and Pali-Aike are between 1.2 and 1.4. In contrast, garnets from gt-sp peridotites display a broader range of mean ARs ranging from 1.7 to 2.3. Mean ARs for gt and gt-sp peridotites are shown in Fig. 10, where they are compared to ARs for cratonic garnet peridotites and in spinel-pyroxene clusters in spinel peridotite xenoliths.

## Discussion

### *Modal abundances of garnet and spinel*

CT-scanning produces 3D volumes of gt-sp and gt peridotite xenoliths which **may** offer a more accurate classification of samples. Calculating modal mineralogy from thin-sections alone may not provide the most accurate classification since clustering of garnets can lead to sections of the sample being devoid of garnet. **Also, gt-sp clusters can co-exist with spinel-free garnets and some samples contain no interstitial spinel.** Therefore, **analysis of slice images and 3D rendered volumes can be used to better characterise a xenolith as a gt or gt-sp peridotite.**

Variation of garnet content seen **in** the 3D volumes is due to clustering of garnet grains in the sample and since the garnets are **general ellipsoidal in shape**, the position of the slice image affects the volume of garnet observed. Based on point counting on a thin-section, sample VI 313 532 was characterised as a gt peridotite (Table 1) but based on the 3D volume slice images, it is **clearly** a gt-sp peridotite due to the presence of significant spinel volume in several gt-sp clusters. Modal mineralogy of sample VI 313 148 also shows a similar presence of **a small volume** of spinel in the CT scan.

### *Garnet-spinel cluster textures*

Micro-CT images of garnet-spinel clusters in peridotite xenoliths **reveal** the complex relationship between garnet and spinel (Figs. 4 - 9). **Spinel** is not just simply an inclusion in garnet but both minerals form complex structures. Slice images of the garnet grains have also **revealed low density silicate inclusions.** EMPA and BSE images of such inclusions in samples VI 313 116 and PA 18 (Fig. 3B) confirmed **that they are olivine.** Thus they record the solid-state reaction of pyroxene and spinel converting to garnet and olivine (equ 1).

The lineation seen in the gt-sp structures (Fig. 4) and **the** ellipsoidal shape of garnet grains and gt-sp clusters point to deformation which **probably** occurred while the rock was garnet-free. **Fig. 10 shows that the highest mean aspect ratios are found in spinel-pyroxene clusters whilst the lowest are found in garnet peridotites.** Garnet grains in **the studied** gt peridotites are somewhat ellipsoidal ( $AR = 1.2-1.4$ ) but **their** overall grain shape is much more spherical compared with the gt-sp structures ( $AR = 1.7-2.3$ ), which in turn are more similar to the shape of spinel-pyroxene clusters in mantle xenoliths from Lanzarote and the Massif Central (Bhanot et al., 2017). A micro-CT study of a garnet peridotite from Kaapvaal craton (not included in this study) shows an average garnet AR of 1.3, remarkably similar to those in spinel-free garnet peridotites in this study. Thus we conclude that the garnet growth occurred after deformation. This may also account for the clustered nature observed in the garnets.

The mineral compositions of the garnet-free peridotites are not systematically different from those of the garnet peridotites and, therefore, the difference in mineral assemblage must depend on the difference in physical conditions under which these peridotites recrystallized (Kushiro and Yoder, 1966). The boundary between the spinel- and garnet-lherzolite mineral facies is strongly curved between 1300°C and 1450°C; below 1200°C it lies almost parallel to the temperature axis on a T-P diagram (O'Hara et al., 1971). Experimental studies of the spinel to garnet transition show that it occurs at ~ 1.6 GPa at 1000°C in the CMAS (CaO-MgO-Al<sub>2</sub>O<sub>3</sub>-SiO<sub>2</sub>) system (Jenkins & Newton, 1979; Ionov et al., 1999; Klemme and O'Neill, 2000). However, the experiments of Robinson and Wood (1998) demonstrated that the minimum pressure at which garnet is stable on the anhydrous solidus of fertile peridotite is 2.8 GPa, corresponding to a depth of about 85 km and the spinel to garnet transition, which is 0.1–0.2 GPa wide, deepens as melt is extracted from the solid residue and solidus temperatures increase. Perkins and Anthony (1999) used bulk rock compositions to calculate equilibrium phase diagrams to calculate the conditions in which mineral assemblages are stable in the upper mantle. This approach requires consideration of the 7-component system SiO<sub>2</sub> – Al<sub>2</sub>O<sub>3</sub> – Cr<sub>2</sub>O<sub>3</sub> – FeO – MgO – CaO – Na<sub>2</sub>O, internally consistent thermodynamic data for end-members, and reliable mixing models for all mineral solutions. They showed that a specific mineral assemblage is stable over a range of P–T conditions and that the compositions of the individual minerals vary with changing P–T conditions, with the ol + cpx + opx + sp + gt five-phase assemblages having a very restricted stability field, i.e. ~0.5 kbar at 1100 °C.

The pressure interval where garnet and spinel coexist in the peridotite mantle beneath Vitim appears to be rather narrow (Ionov et al., 1993), when uncertainties of the geobarometry (Brey & Kohler, 1990) are considered. The garnet-spinel peridotites yield pressure estimates ranging from 1.6 to 1.95 GPa (980°C < T < 1045°C). This indicates a 'garnet-in' pressure of 1.6–1.7 GPa and a 'spinel-out' limit (for fertile peridotites) of ~2.0 GPa for Vitim xenoliths. Figure 11 is a pressure-temperature graph of equilibrium temperatures and pressures for gt and gt-sp peridotites from Vitim and Pali-Aike. The graph shows a distinction between phase assemblages where gt peridotites from Vitim plot in the high pressure (garnet) stability field whilst gt-sp peridotites plot in the relatively cooler and lower pressure region.

Garnet-spinel peridotites from Pali-Aike plot at a higher pressure than those from Vitim.

Mantle xenoliths record the fact that different continental settings display mineralogical variations in relation to the age of the overlying crust; older sub-continental lithospheric mantle shows an increasing level of depletion indicated by low values of CaO and Al<sub>2</sub>O<sub>3</sub> in bulk rocks. Thus, Archean lithospheric mantle has a high Mg# (generally 93–95) coupled with low CaO and Al<sub>2</sub>O<sub>3</sub> contents. In contrast Proterozoic

and Phanerozoic sub-continental lithospheric mantle shows intermediate Mg# values and higher CaO and  $\text{Al}_2\text{O}_3$  bulk rock compositions. Depletion trends in mantle xenoliths thus record the mean level of depletion in the sub-continental lithospheric mantle from the Archean to the Phanerozoic (Artemieva, 2011). In mantle-derived garnet peridotite xenoliths, the  $\text{Cr}_2\text{O}_3$  content of garnet is correlated with generally accepted measures of depletion in basaltic components and high-Cr garnets are found in refractory rocks with high Mg#, low CaO and  $\text{Al}_2\text{O}_3$ , whereas low-Cr garnets are found in more fertile peridotites (Griffin et al., 1999).  $\text{Cr}_2\text{O}_3$  content of garnets from Vitim and Pali Aike are low, with a mean Cr# of 20 for Vitim and 28 for Pali Aike, whereas cratonic garnet Cr#s are generally ~65. CaO content in garnets from Vitim and Pali Aike range between 4.8-5.1 wt% and are thus distinct from the Cr- and Ca-rich garnets found in Kaapvaal-type (cratonic) peridotites.

In Fig. 3a, Vitim and Pali Aike peridotites plot within the lower part of the mantle array whilst cratonic peridotites occupy the more depleted (higher Cr# and Mg#) part of the array. Comparison of gt Mg# and Cr# (Fig. 3b) reveals a distinct difference between the more depleted cratonic garnets and the low-Cr garnets of the younger Pali Aike and Vitim. Based on modal cpx content and the mantle array diagram, the Pali Aike mantle is more depleted than the lithospheric mantle of Vitim.

Estimated equilibration temperatures and pressures for Vitim and Pali Aike were calculated using the Ca-opx thermometer of Brey and Köhler (1990) and the barometer of Nickel and Green (1985) and presented in the PT diagram in Figure 12, with additional data for Vitim from the study by Ionov et al (2005) and for Pali Aike from Wang et al (2008). Garnet spinel peridotites from both Pali Aike and Vitim occupy a region close to the oceanic geotherm ( $65 \text{ mW/m}^2$ ) and show a narrow range of pressure and temperature, i.e. 18.4-23.2 kbar and 965-1121 °C. Cratonic peridotites from Kaapvaal (Simon et al., 2003) plot at greater depth (~ 125 km), display a wider range in temperature and pressure in comparison to both Vitim and Pali Aike, and plot close to the continental geotherm estimated at  $40 \text{ mW/m}^2$ . Ionov et al (2005) stated that, assuming that temperature gradually increases with depth, the relative positions of the rock types in the lithospheric cross-section beneath Vitim can be inferred. Garnet–spinel peridotites coexist with spinel peridotites in the depth range ~60–70 km (18–21 kbar). Spinel peridotites, garnet–spinel and garnet peridotites occur together in the depth range ~70–75 km (21–22 kbar). Above 22 kbar garnet peridotite begins to dominate.

Garnet, garnet–spinel and spinel peridotites can coexist at pressures of 18–22 kbar because of differences in their bulk major element compositions, since the spinel–garnet phase transition takes place at greater depths in more refractory rocks (Ionov et al., 2005). Robinson and Wood (1998) also

pointed out that the spinel to garnet transition deepens as melt is extracted from the solid residue and solidus temperatures increase. This is probably why Pali Aike gt-sp peridotite samples plot with higher pressures than those from Vitim (Fig. 11).

The 3D volume of sample PA 31 from Pali-Aike displays a halo which surrounds spinel but not garnet. The halo is a phase denser than the silicate phase but significantly less dense than spinel and less dense than garnet. The halos are not isolated but appear to connect to channels and provide textural evidence of metasomatic reactions affecting the mantle. This phase is probably clinopyroxene.

Textures of single spinel-pyroxene complex structures in spinel peridotites from Lanzarote and Massif Central were investigated by Bhanot et al. (2017). Sizes of these structures range from 4 to 12 mm in the longest dimension. Their AR values range from 2.0 to 2.9. Their ellipsoid shape is attributed to flattening of originally spherical structures formed by replacement of large, originally equant, garnets with a spinel-pyroxene cluster (Bhanot et al., 2017). Gt-sp structures from Vitim and Pali-Aike display a similar ellipsoidal shape. Garnet grains in garnet peridotites from Vitim and Pali-Aike (PA18 and VI313116, Figs. 7 and 9B) also show ellipsoidal shapes but with a lower AR. The ellipsoidal shape of the gt-sp structures reflect the shape and size of the original deformed spinel-pyroxene clusters, whereas the newly grown garnets have a more spherical shape.

Garnets in micro-CT images of gt-spinel peridotites are visualized as separate grains with no evidence of chemical zoning relating to the kelyphite rim and its formation. Garnet and the associated complex spinel structure are very similar to spinel textures observed in spinel peridotite xenoliths from Massif Central and Lanzarote (Bhanot et al., 2017), albeit the spinel structures in PA and VI are less vermicular. Thus, they are considered to be relics of the original more vermicular spinel complex in a spinel-pyroxene cluster. Based on this observation, it is likely that the textures are related and thus act as examples of the garnet + olivine reaction with garnet ( $\pm$  ol inclusions) and spinel-pyroxene clusters are examples of the reversible sub-solidus reaction ( $\text{sp} + \text{opx} + \text{cpx} \leftrightarrow \text{ol} + \text{gt}$ ) going to completion, whereas the gt-sp textures seen in this study represent the transition stage of that reaction.

In addition, the size and texture of the spinel is relative to the degree of completion of the reaction, with less complex vermicular spinel textures representing the reaction near to completion (along with ol inclusions) relative to the more complex and more substantial spinel volume of the gt-sp cluster (PA 16). 3D rendered images of garnet grains show no concentric pattern, garnet appears as a single crystal with no evidence of distinct chemical zoning. The upper mantle beneath both Vitim and Pali-Aike has been

subjected to cooling and Ionov (2004) and Stern et al (1999) have proposed cooling of the lithosphere as the driving force for the development of gt and gt-sp peridotite textures. The 3D rendered volumes of both gt peridotites and gt-sp peridotites reveal that there is no interaction between the kelyphite rim and conversion of the original spinel-pyroxene cluster to garnet. Therefore, this process of kelyphite rim reaction forms no part of the gt-sp cluster formation process.

## Conclusions

CT scanning of garnet-spinel and garnet peridotite xenoliths from Vitim (Russia) and Pali-Aike (Patagonia) provides accurate representations of the textures of the constituent garnets and spinels. The complex textures shown in the 3D volumes reveal the tectonic histories of the upper mantle beneath the two localities. Garnets containing olivine inclusions and complex garnet-spinel structures are considered to be the products of the reaction between pyroxene and spinel ( $sp + opx + cpx \leftrightarrow ol + gt$ ). We have interpreted the textures to be evidence of a multi-stage process affecting the upper mantle. This process involves several stages. Firstly, the original garnet-bearing mantle was decompressed due to lithospheric thinning and followed the reverse reaction in equ 1 such that the garnet (and olivine) was transformed into spinel-pyroxene clusters. These clusters then experienced a period of deformation which changed their shapes to ellipsoids with aspect ratios of 2.0-2.9, similar to those of spinel-pyroxene clusters in other mantle xenoliths. We interpret the lineation of garnet-spinel clusters seen in sample PA 10 as deformation formed during the garnet-free phase and retained as the garnets grew. The final stage involves cooling and/or thickening of the lithosphere (Fig. 13) which transformed the spinel-pyroxene clusters back to garnet and olivine. Garnet-spinel clusters are interpreted to represent the incomplete conversion of a spinel-pyroxene cluster to garnet + olivine. Following conversion of spinel to garnet, garnet-spinel peridotites experienced metasomatic reactions as seen in the halo textures in sample PA 31. Finally, garnets were mantled with kelyphite rims due to increased heating prior to exhumation. We predict that the gt-sp cluster textures seen in Vitim and Pali-Aike gt-sp peridotites will form in regions which have experienced lithospheric thinning followed by isobaric cooling of the lithosphere.

## Acknowledgments

We thank Dimitri Ionov and Theo Ntaflos for providing samples from Vitim; the NHM (London) is thanked for providing samples from Pali-Aike, deposited by Pamela Kempton. We are also grateful to the X-ray CT scan facility at the Natural History Museum for CT data collection and help and advice provided in data processing. We thank Andy Beard for thin-section preparation and help and advice he provided with microprobe analysis. Krishan Bhanot would like to take this opportunity to thank Michael Hippler and Matthew Clarke at Rigaku Europe SE for financing his PhD project. We also thank the two anonymous reviewers and the editor Alan Woodland for their helpful comments.

## References

- Artemieva, I., 2011. Lithosphere: an interdisciplinary approach. Cambridge University Press.
- Bhanot, K.K., Downes, H., Petrone, C.M. and Humphreys-Williams, E., 2017. Textures in spinel peridotite mantle xenoliths using micro-CT scanning: Examples from Canary Islands and France. *Lithos*, 276, 90-102.
- Boyd, F.R., Pokhilenko, N.P., Pearson, D.G., Mertzman, S.A., Sobolev, N.V. and Finger, L.W., 1997. Composition of the Siberian cratonic mantle: evidence from Udachnaya peridotite xenoliths. *Contributions to Mineralogy and Petrology*, 128(2-3), 228-246.
- Brey, G.P. and Köhler, T., 1990. Geothermobarometry in four-phase lherzolites II. New thermobarometers, and practical assessment of existing thermobarometers. *Journal of Petrology*, 31(6), 1353-1378.
- Cao, R.L. and Zhu, S.H., 1987. Mantle xenoliths and alkali-rich host rocks in eastern China. *Mantle xenoliths* (Ed P H Nixon), pp.168-180.
- Carlson W D, T. Rowe T, Ketcham R A, M. W. Colbert M W 2003. Applications of high-resolution X-ray computed tomography in petrology, meteoritics and palaeontology. *Geological Society London, Special Publications* 215, 7-22
- Carswell, D.A., Clarke, D.B. and Mitchell, R.H., 1979. The petrology and geochemistry of ultramafic nodules from Pipe 200, northern Lesotho. *The Mantle Sample: Inclusion in Kimberlites and Other Volcanics*, 16, 127-144.
- Douglas, B.J., Saul, S.L. and Stern, C.R., 1987. Rheology of the upper mantle beneath southernmost South America inferred from peridotite xenoliths. *The Journal of Geology*, 95(2), 241-253.
- Gibson, S.A., McMahon, S.C., Day, J.A. and Dawson, J.B., 2013. Highly refractory lithospheric mantle beneath the Tanzanian craton: evidence from Lashaine pre-metasomatic garnet-bearing peridotites. *Journal of Petrology*, 54(8), 1503-1546.
- Godard, G. and Martin, S., 2000. Petrogenesis of kelyphites in garnet peridotites: a case study from the Ulten zone, Italian Alps. *Journal of Geodynamics*, 30(1-2), 117-145.

512 Green, D.H. and Ringwood, A.E., 1967. The stability fields of aluminous pyroxene peridotite and garnet  
513 peridotite and their relevance in upper mantle structure. *Earth and Planetary Science Letters*, 3, 151-  
514 160.

515 Grégoire, M., Bell, D.R. and Le Roex, A.P., 2003. Garnet lherzolites from the Kaapvaal Craton (South  
516 Africa): trace element evidence for a metasomatic history. *Journal of Petrology*, 44(4), 629-657.

517 Ionov, D., 2002. Mantle structure and rifting processes in the Baikal–Mongolia region: geophysical data  
518 and evidence from xenoliths in volcanic rocks. *Tectonophysics*, 351(1-2), 41-60.

519 Ionov, D., 2004. Chemical variations in peridotite xenoliths from Vitim, Siberia: inferences for REE and Hf  
520 behaviour in the garnet-facies upper mantle. *Journal of Petrology*, 45(2), 343-367.

521 Ionov, D.A. and Hofmann, A.W., 2007. Depth of formation of subcontinental off-craton peridotites. *Earth  
522 and Planetary Science Letters*, 261(3), 620-634.

523 Ionov, D.A., Ashchepkov, I. and Jagoutz, E., 2005. The provenance of fertile off-craton lithospheric  
524 mantle: Sr–Nd isotope and chemical composition of garnet and spinel peridotite xenoliths from Vitim,  
525 Siberia. *Chemical Geology*, 217(1-2), 41-75.

526 Ionov, D.A., Ashchepkov, I.V., Stosch, H.G., Witt-Eickschen, G. and Seck, H.A., 1993. Garnet peridotite  
527 xenoliths from the Vitim volcanic field, Baikal region: the nature of the garnet-spinel peridotite  
528 transition zone in the continental mantle. *Journal of Petrology*, 34(6), 1141-1175.

529 Ionov, D.A., Doucet, L.S. and Ashchepkov, I.V., 2010. Composition of the lithospheric mantle in the  
530 Siberian craton: new constraints from fresh peridotites in the Udachnaya-East kimberlite. *Journal of  
531 Petrology*, 51(11), 2177-2210.

532 Jenkins, D.M. and Newton, R.C., 1979. Experimental determination of the spinel peridotite to garnet  
533 peridotite inversion at 900 C and 1,000 C in the system CaO–MgO–Al<sub>2</sub>O<sub>3</sub>–SiO<sub>2</sub>, and at 900 °C with natural  
534 garnet and olivine. *Contributions to Mineralogy and Petrology*, 68(4), 407-419.

535 Kempton, P.D., Lopez-Escobar, L., Hawkesworth, C.J., Pearson, D.G., Wright, D.W. and Ware, A.J., 1999.  
536 Spinel ± garnet lherzolite xenoliths from Pali Aike: Part 1. Petrography, mineral chemistry and  
537 geothermobarometry. *JB Dawson volume. Proceedings of VIIth International Kimberlite Conference*, pp.  
538 403-414.

539 Ketcham R A and Carlson W D. 2001. Acquisition, optimization and interpretation of X-ray computed  
540 tomographic imagery: applications to the geosciences. *Computers & Geosciences* 27, 381–400.

541 Klemme, S. and O'Neill, H.S., 2000. The near-solidus transition from garnet lherzolite to spinel lherzolite.  
542 *Contributions to Mineralogy and Petrology*, 138(3), 237-248.

543 Kruth J P, M. Bartscher M. Carmignato Schmitt R, De Chiffre L, Weckenmann A. 2011. Computed  
544 tomography for dimensional metrology. *CIRP Annals - Manufacturing Technology* 60, 821–842

545 Kushiro, I. and Yoder Jr, H.S., 1966. Anorthite-forsterite and anorthite-enstatite reactions and their  
546 bearing on the basalt-eclogite transformation. *Journal of Petrology*, 7(3), 337-362.

547 Mercier, J.C. and Nicolas, A., 1975. Textures and fabrics of upper-mantle peridotites as illustrated by  
548 xenoliths from basalts. *Journal of Petrology*, 16(1), 454-487.



549 Murav'yeva, N.S., Polyakov, A.I. and Senin, V.G., 1985. Physicochemical conditions and mechanism of  
550 formation of garnet-spinel lherzolite from the Vitim Plateau, Baikal rift zone. Doklady Akademii Nauk  
551 SSSR, 283, 1458-1462.

552 Nickel, K.G. and Green, D.H., 1985. Empirical geothermobarometry for garnet peridotites and  
553 implications for the nature of the lithosphere, kimberlites and diamonds. *Earth and Planetary Science*  
554 *Letters*, 73(1), 158-170.

555 O'Hara, M.J., Richardson, S.W. and Wilson, G., 1971. Garnet-peridotite stability and occurrence in crust  
556 and mantle. *Contributions to Mineralogy and Petrology*, 32(1), 48-68.

557 Perkins, D. and Anthony, E.Y., 2011. The evolution of spinel lherzolite xenoliths and the nature of the  
558 mantle at Kilbourne Hole, New Mexico. *Contributions to Mineralogy and Petrology*, 162(6), 1139-1157.

559 Petit, C., Koulakov, I. and Deverchère, J., 1998. Velocity structure around the Baikal rift zone from  
560 teleseismic and local earthquake traveltimes and geodynamic implications. *Tectonophysics*, 296(1-2),  
561 125-144.

562 Ramakrishna K, Muralidhar, and P Munshi K. 2006. Beam-hardening in simulated X-ray tomography. *NDT*  
563 *& E International*, 39, Pp 449–457.

564 Reid, A.M., Donaldson, C.H., Brown, R.W., Ridley, W.I. and Dawson, J.B., 1975. Mineral chemistry of  
565 peridotite xenoliths from the Lashaine volcano, Tanzania. In *Physics and Chemistry of the Earth*, 525-  
566 543. Pergamon.

567 Robinson, J.A.C. and Wood, B.J., 1998. The depth of the spinel to garnet transition at the peridotite  
568 solidus. *Earth and Planetary Science Letters*, 164(1-2), 277-284.

569 Simon, N.S., Irvine, G.J., Davies, G.R., Pearson, D.G. and Carlson, R.W., 2003. The origin of garnet and  
570 clinopyroxene in “depleted” Kaapvaal peridotites. *Lithos*, 71(2-4), 289-322.

571 Skewes, M.A. and Stern, C.R., 1979. Petrology and geochemistry of alkali basalts and ultramafic  
572 inclusions from the Palei-Aike volcanic field in southern Chile and the origin of the Patagonian plateau  
573 lavas. *Journal of Volcanology and Geothermal Research*, 6(1-2), 3-25.

574 Smith, D., 1977. The origin and interpretation of spinel-pyroxene clusters in peridotite. *The Journal of*  
575 *Geology*, 85(4), 476-482.

576 Stern, C.R., Kilian, R., Olker, B., Hauri, E.H. and Kyser, T.K., 1999. Evidence from mantle xenoliths for  
577 relatively thin (< 100 km) continental lithosphere below the Phanerozoic crust of southernmost South  
578 America. In: *Developments in Geotectonics*, 24, 217-235.

579 Wang, J., Hattori, K.H., Li, J. and Stern, C.R., 2008. Oxidation state of Paleozoic subcontinental  
580 lithospheric mantle below the Pali Aike volcanic field in southernmost Patagonia. *Lithos*, 105(1-2), 98-  
581 110.

582

583 Figure Captions

584

585 Fig. 1a. Garnet peridotite thin-section PPL image (VI 313 532). Garnet grains are mantled by  
586 kelyphite rims. Scalebar is 5mm. Fig. 1b. Garnet-spinel peridotite thin-section PPL image (PA  
587 16). Garnet-spinel clusters display complex vermicular structures and are mantled by a  
588 kelyphite rim. Scalebar is 5mm.

589 Fig. 2a. BSE image of gt-sp cluster and kelyphite rim (PA 16). Fig. 2b. BSE image of garnet with ol  
590 inclusion and kelyphite rim in a garnet peridotite (PA 18). Scale bar 1mm.

591 Fig. 3a. OSMA diagram for sp peridotites and gt-sp peridotites from Vitim, Pali-Aike and cratonic  
592 peridotites. Data taken from this study and Ionov et al., 2005; Ionov et al., 2010; Gibson et al.,  
593 2013 and Simon et al., 2003. Cratonic peridotites are shown as solid diamond, Pali Aike sp  
594 harzburgites as solid circles, Vitim sp lherzolites as open circles, Pali Aike gt-sp peridotites as  
595 solid squares and Vitim gt-sp peridotites as open squares. Fig. 3b. Cr# vs mg# in garnets in Vitim  
596 (open circle) and Pali Aike (solid circle) xenoliths compared with cratonic peridotites (solid  
597 diamond). Cratonic peridotite data taken from Carswell et al., 1979; Grégoire et al., 2003; Ionov  
598 et al., 2010; Gibson et al., 2013; Reid et al., 1975 and Simon et al., 2003.

599 Fig. 3. 3D rendered image of gt-sp cluster in sample PA 10. Garnet coloured yellow, spinel  
600 shown as red. Scalebar is 10mm.

601 Fig 4. Series of 3D rendered images of gt-sp cluster (PA 16) with increasing garnet transparency.  
602 Garnet coloured yellow, spinel shown as red. Scale bar is 3.585 mm.

603 Fig. 5. 3D rendered image of gt-sp cluster (PA 13). Garnet coloured yellow, spinel shown as red.  
604 Scalebar is 4.033 mm.

605 Fig. 6. 3D rendered image of gt-sp cluster (PA 18). Garnet coloured yellow, spinel shown as red.  
606 Scale bar is 7.58 mm.

607 Fig. 7a. 3D rendered image of gt-sp cluster (PA 31). Garnet coloured yellow, spinel shown as  
608 red. Scale bar is 12.28mm. Fig 8b. 3D rendered image of gt-sp cluster (PA 31) with a  
609 metasomatic halo encasing gt-sp clusters. Garnet coloured yellow, spinel shown as red and  
610 metasomatic halo shown as green. Scale bar is 5mm.

611 Fig. 9a. 3D rendered image of garnet grains in **gt peridotite VI 313 1270**. Garnet coloured  
612 yellow. Scale bar is 10 mm. Fig. 9b. 3D rendered image of gt-sp cluster (VI 313 532), garnet  
613 coloured yellow and spinel red. Scale bar is 10 mm.

614 **Fig. 10. Box and whisker plot of aspect ratios (AR) for spinel peridotites from Massif Central**  
615 **(France), Lanzarote (Spain) and Calatrava (Spain) containing spinel-pyroxene clusters, and for gt**  
616 **peridotites and gt-sp peridotites from Vitim (Russia) and Pali Aike. Aspect ratios for garnet in gt**  
617 **peridotites from Kaapvaal craton included for comparison. Mean ARs are shown as a solid black**  
618 **circle.**

619 **Fig. 11. Graph of equilibrium temperatures** and pressures for gt and gt-sp peridotites from  
620 Vitim and Pali-Aike. Data from Ionov et al. (1993), Wang et al. (2008). **Representative gt-sp**

621 transition from Green and Ringwood (1967). Vitim gt lherzolites, solid square, Vitim gt-sp  
622 lherzolites, open square, Pali Aike gt-sp lherzolites, open circle. Temperatures and pressures  
623 calculated using Brey and Köhler (1990) Ca-in-Opx thermometer.

624 Fig. 12. P-T diagram comparing mantle peridotites from Pali-Aike (open square) and Vitim (open  
625 circle), sp peridotites (Vitim, cross) with cratonic mantle xenoliths (open diamonds). Data from  
626 Simon et al. (2003); Ionov et al. (2005) and Wang et al. (2008). Temperatures and pressures  
627 calculated using Brey and Köhler (1990) Ca-in-Opx thermometer, and Nickel and Green (1985)  
628 Al-in-Opx barometer. Gt-sp transition from Green and Ringwood (1967) is representative only,  
629 as this varies in depth according to the composition of the mantle.

630 Figure 13. Mantle facies diagram showing schematic transition of sp peridotite to gt peridotite  
631 stability field by a decrease in pressure (1) followed by isobaric cooling (2) and exhumation (3).  
632 Adapted from Perkins and Anthony (2011).

633



Figure 1  
[Click here to download high resolution image](#)

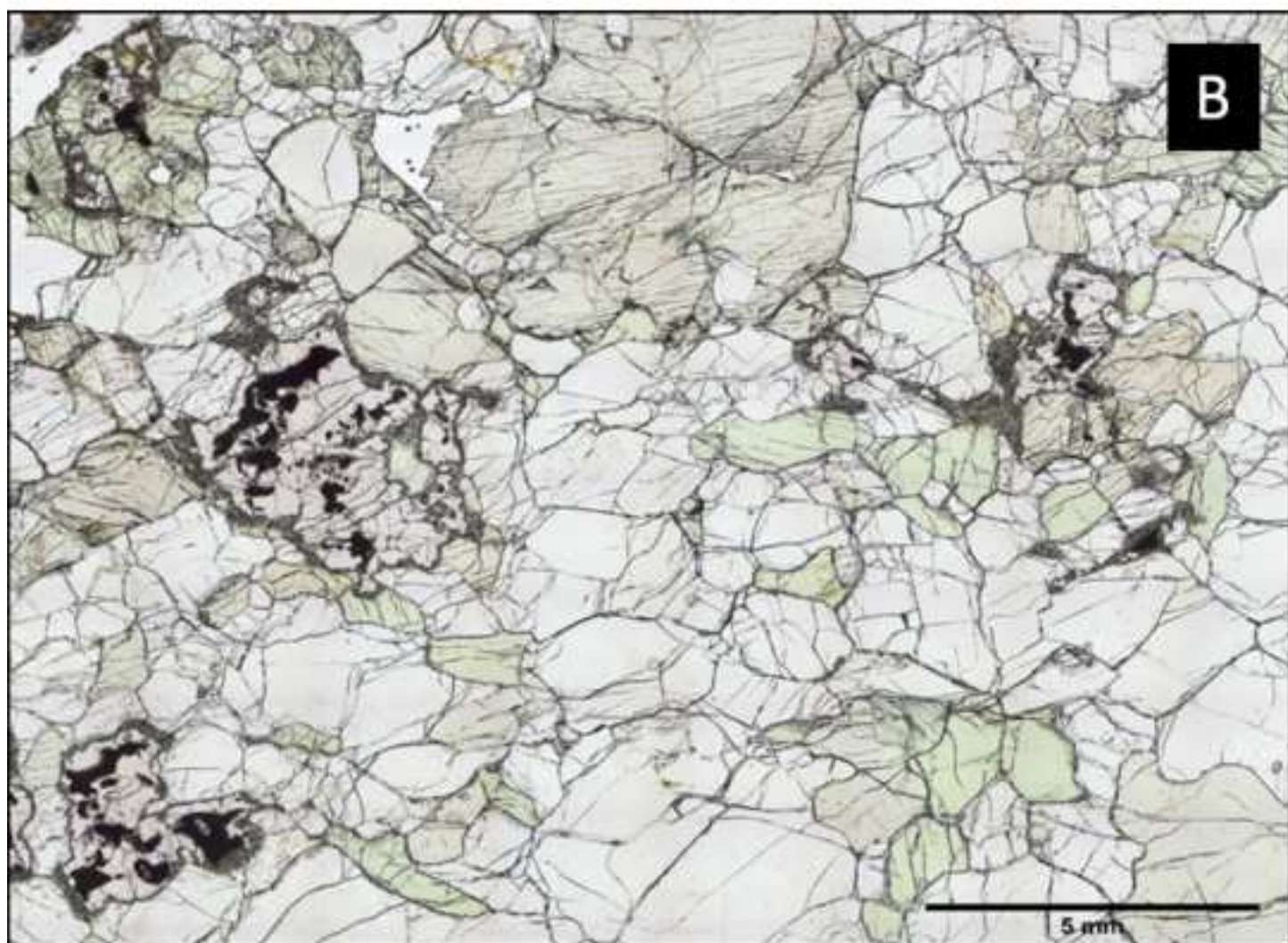


Figure 2  
[Click here to download high resolution image](#)

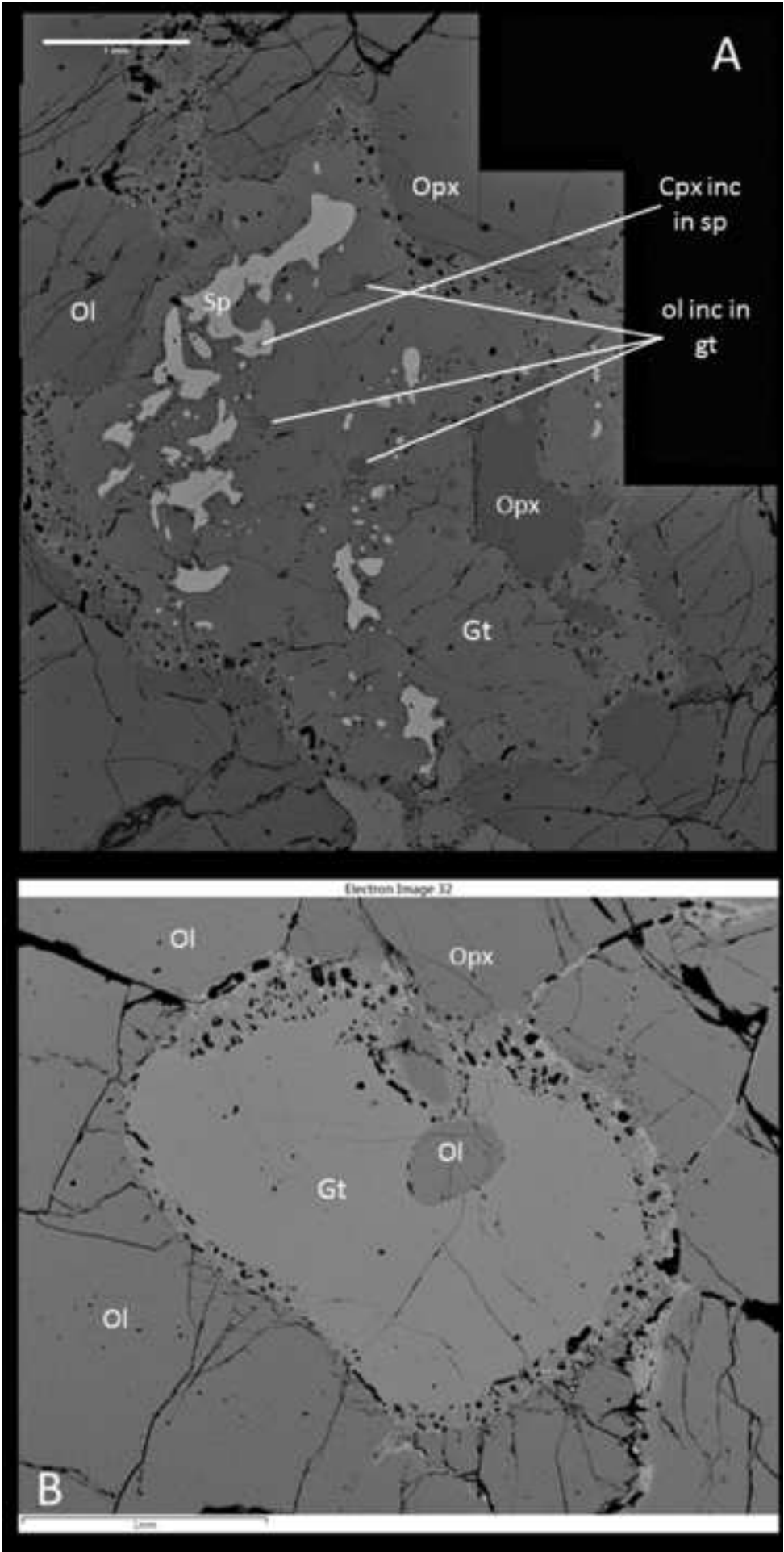


Figure 3  
[Click here to download high resolution image](#)

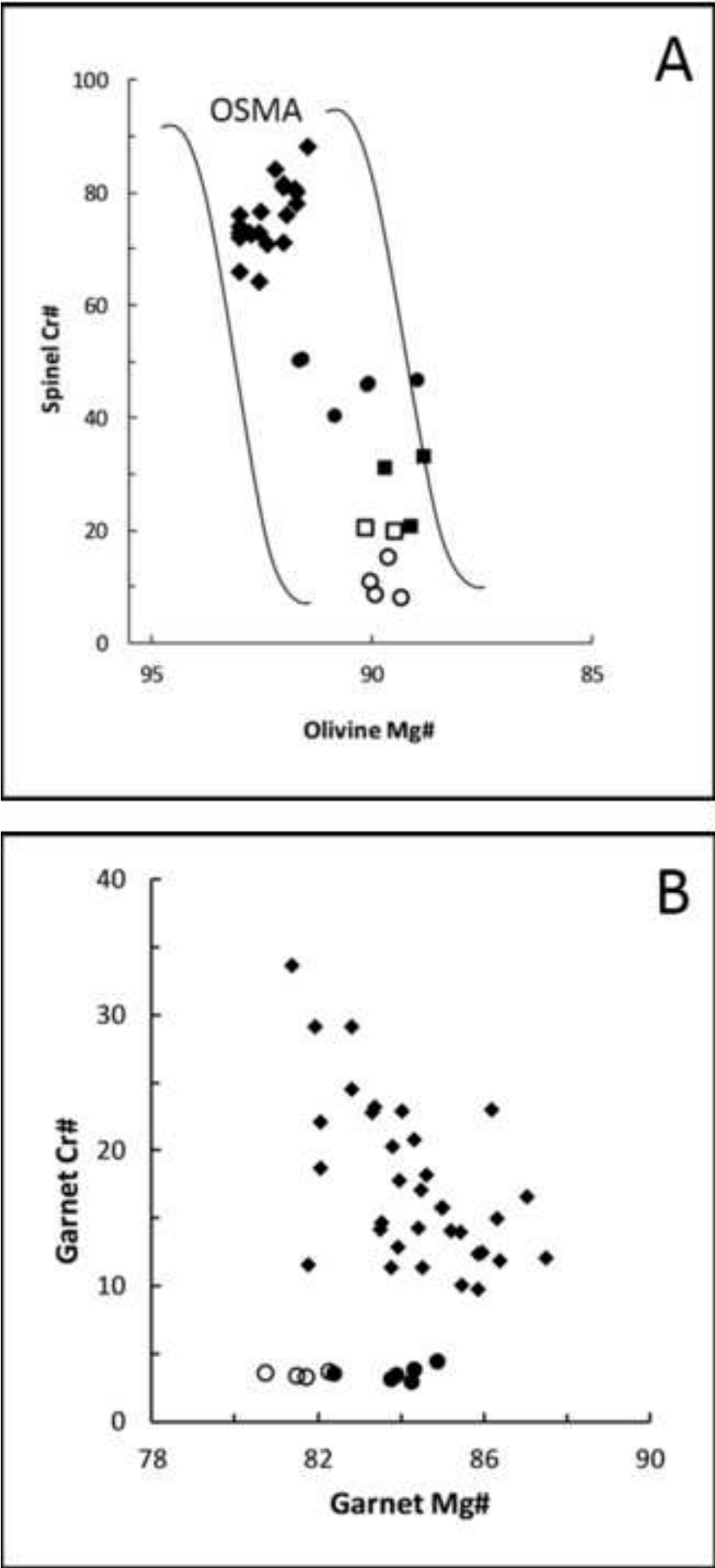




Figure 4  
[Click here to download high resolution image](#)

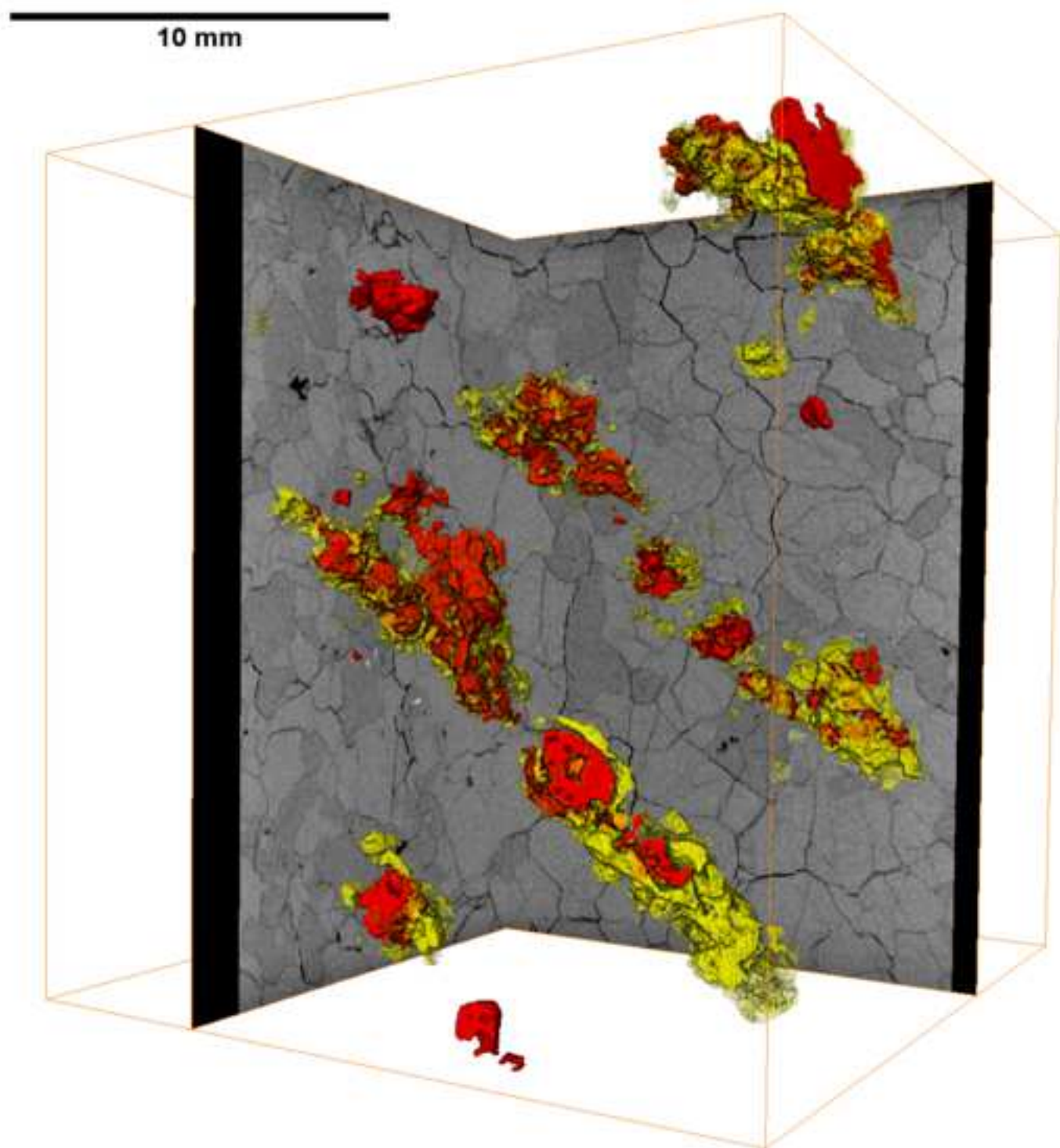


Figure 5  
[Click here to download high resolution image](#)

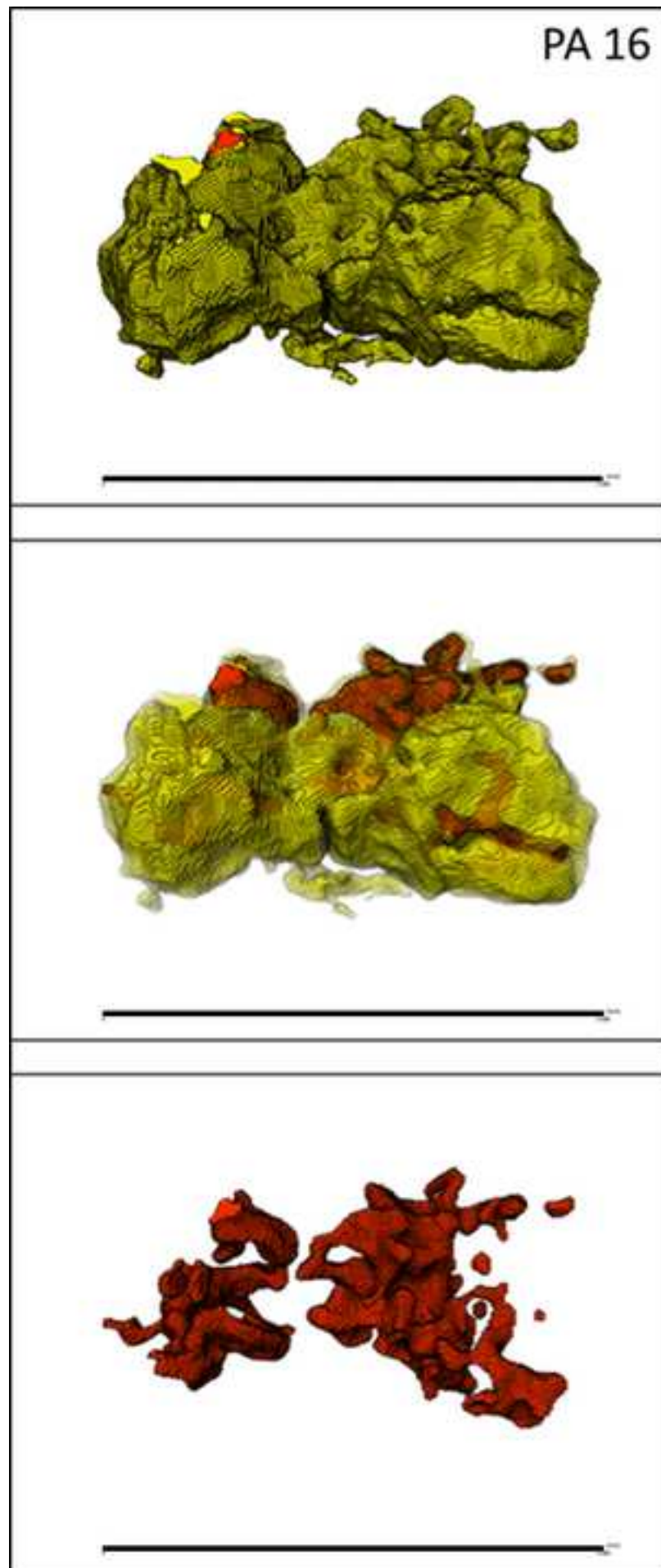




Figure 6  
[Click here to download high resolution image](#)

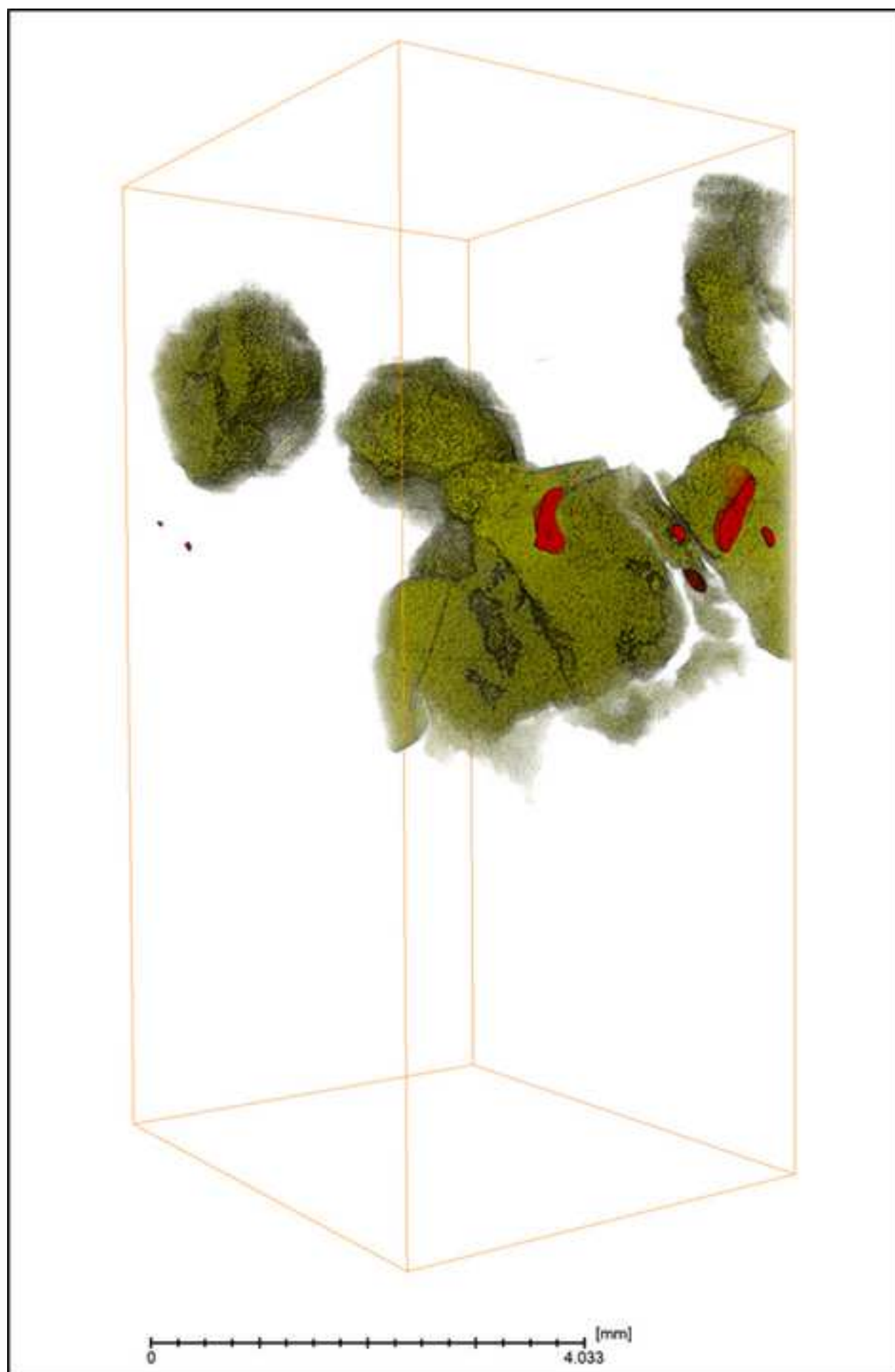


Figure 7  
[Click here to download high resolution image](#)



Figure 8  
[Click here to download high resolution image](#)

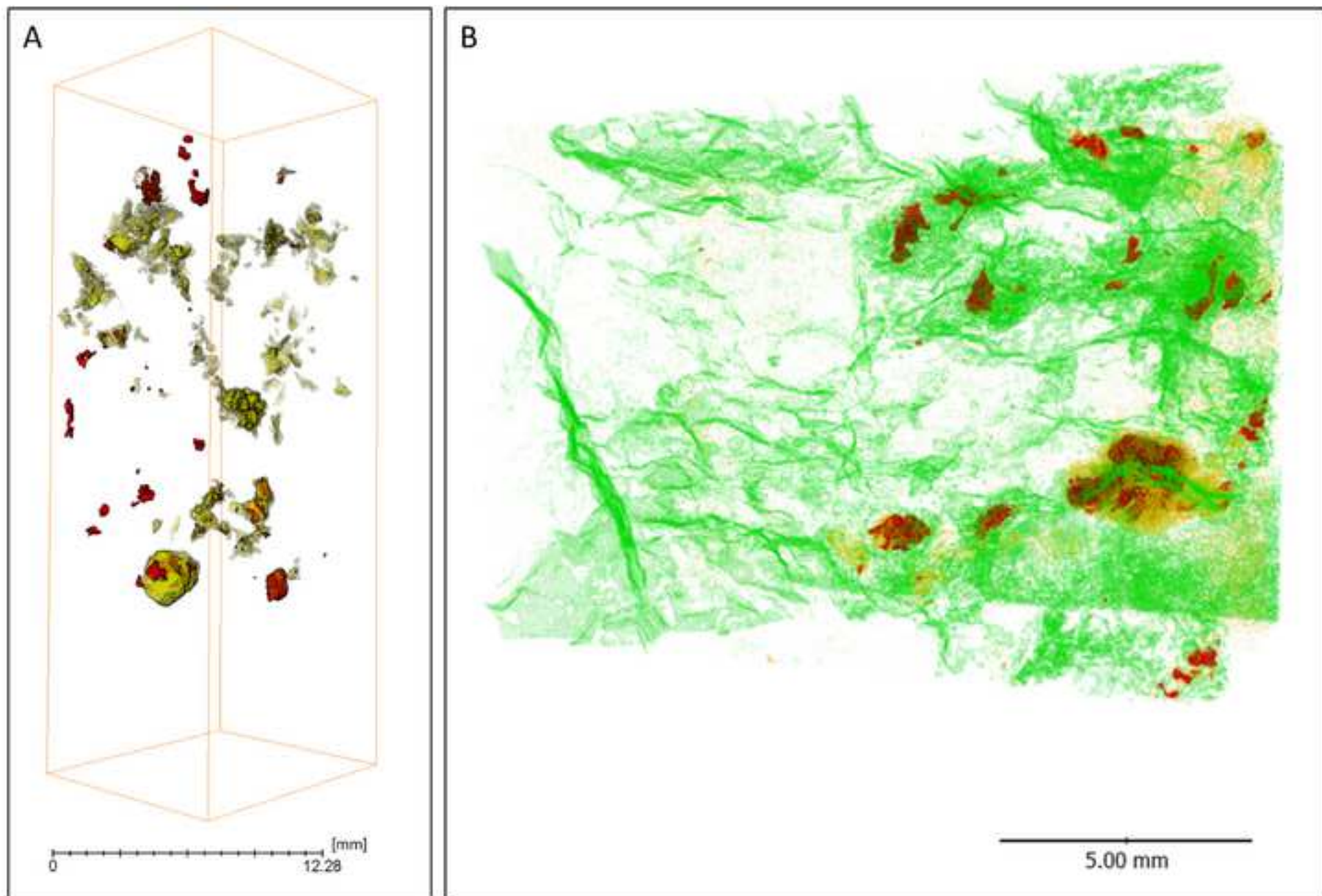




Figure 9  
[Click here to download high resolution image](#)

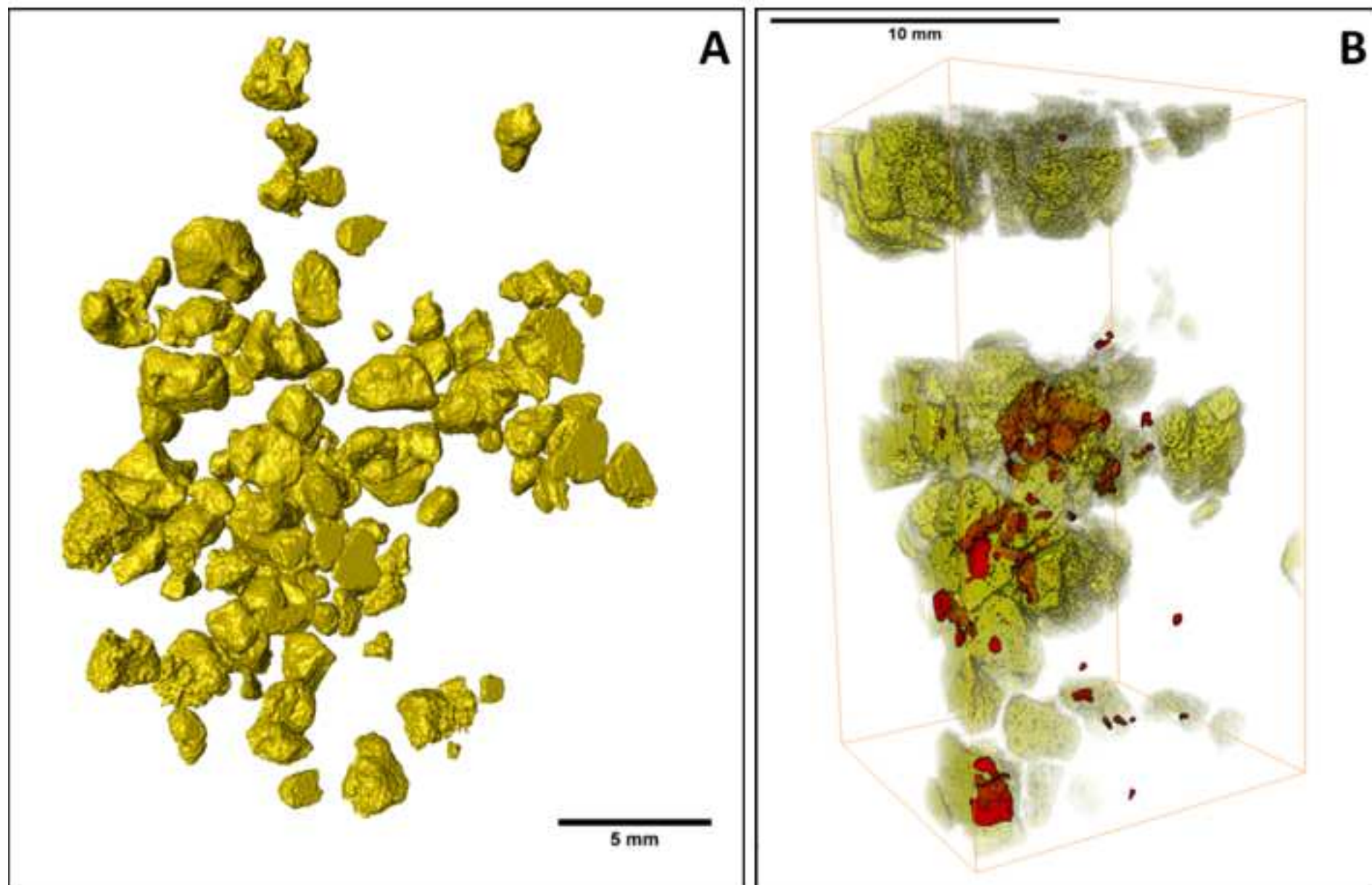


Figure 10 revised  
[Click here to download high resolution image](#)

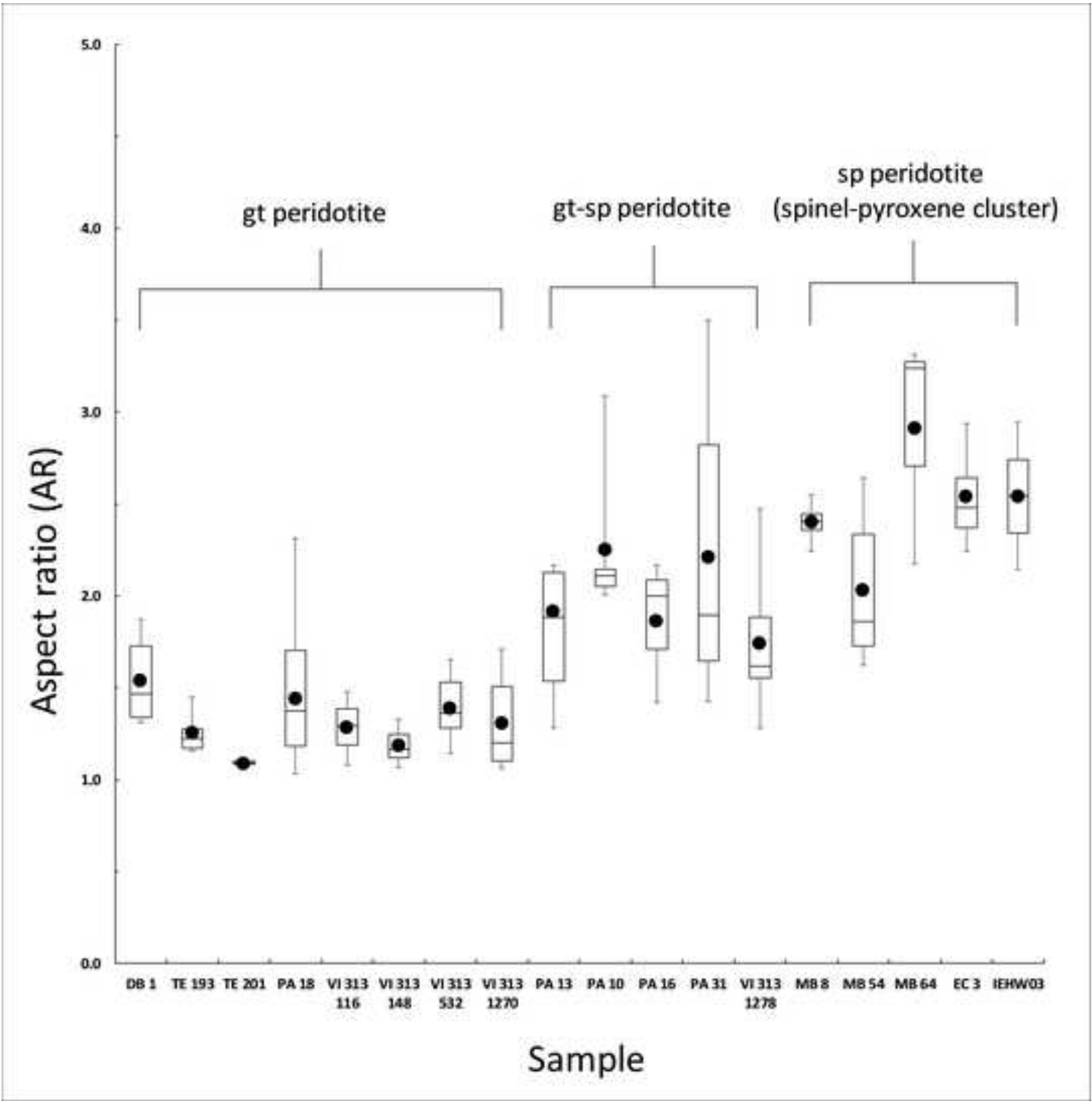


Figure 11 revised  
[Click here to download high resolution image](#)

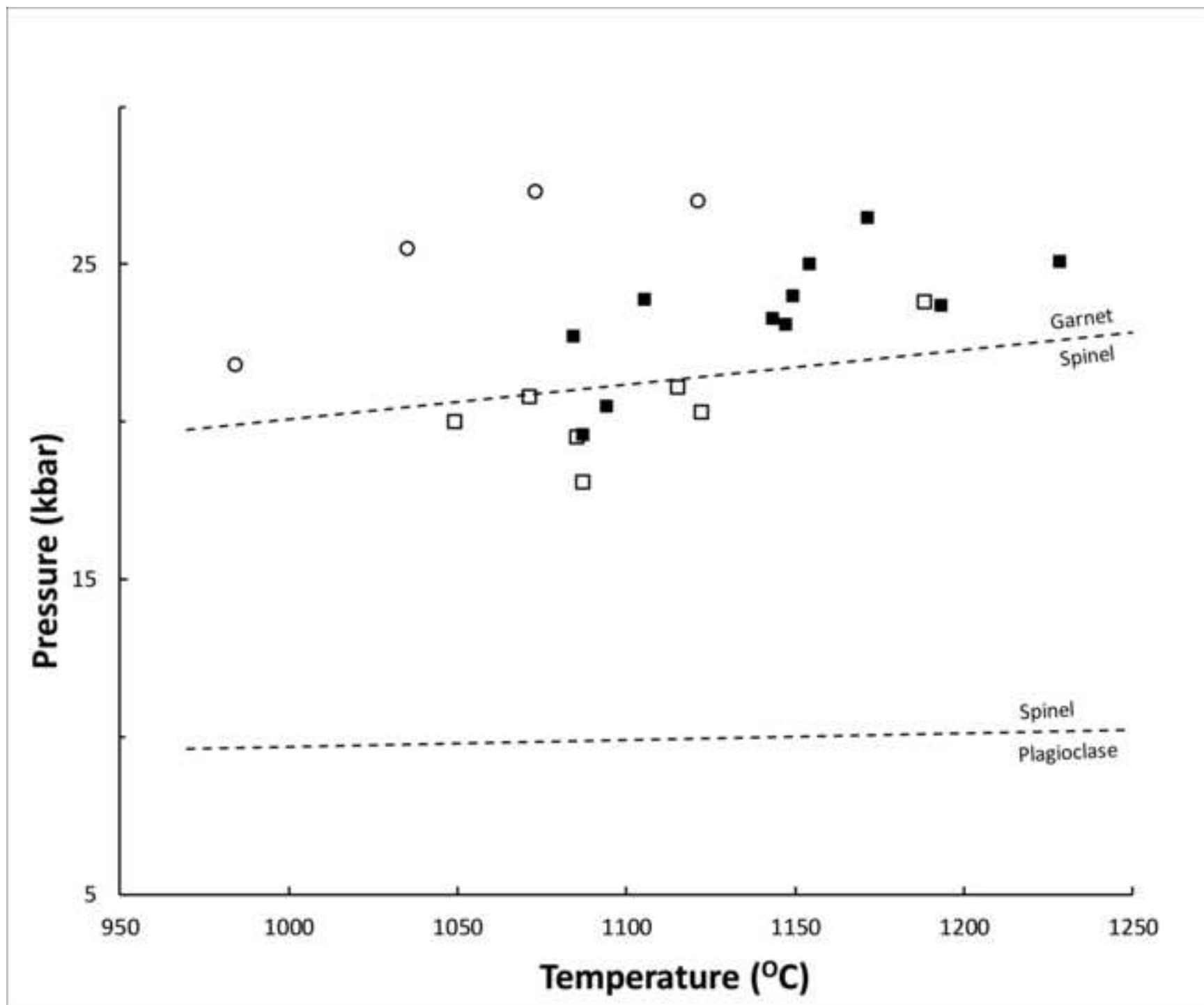


Figure 12  
[Click here to download high resolution image](#)

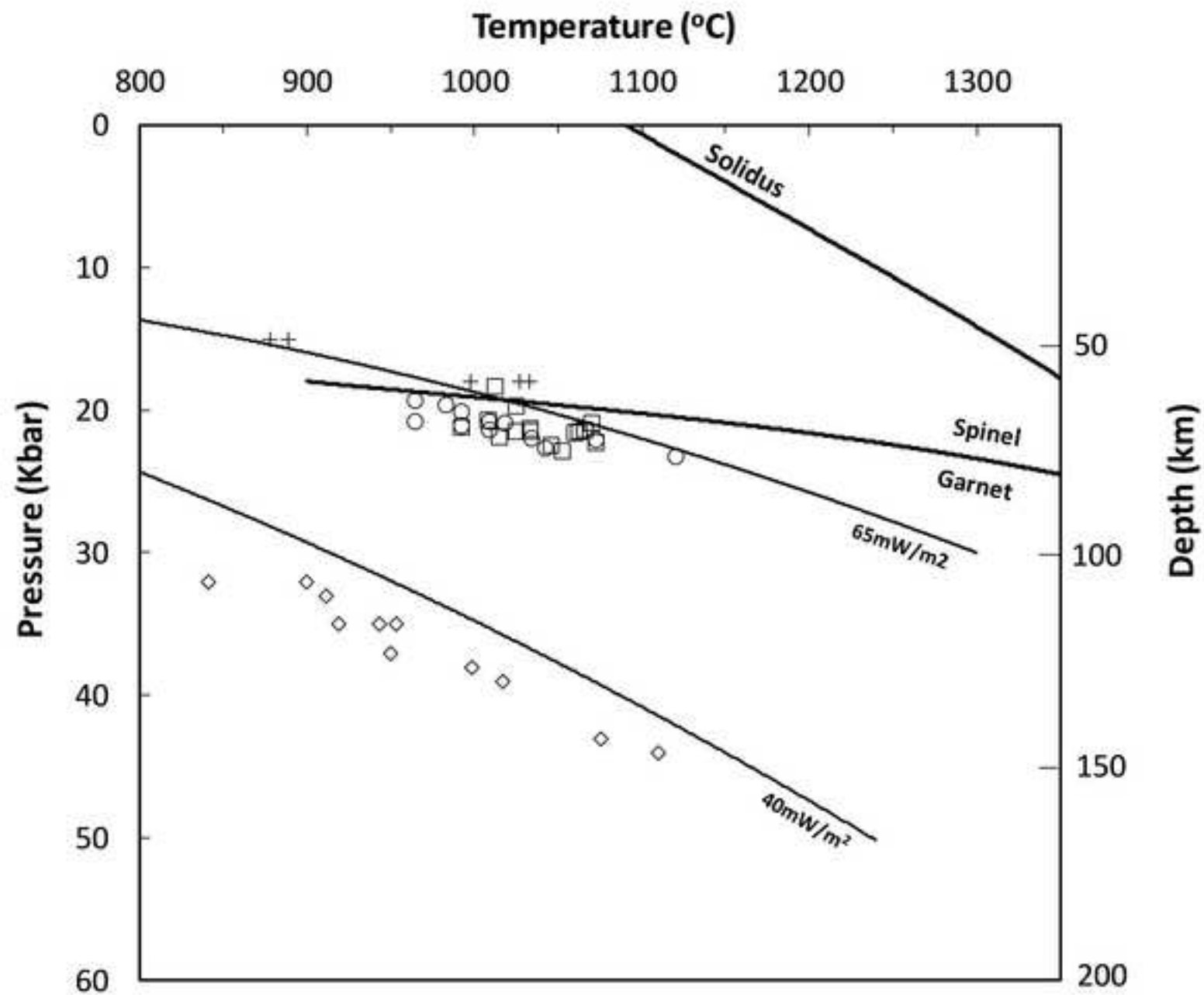


Figure 13  
[Click here to download high resolution image](#)

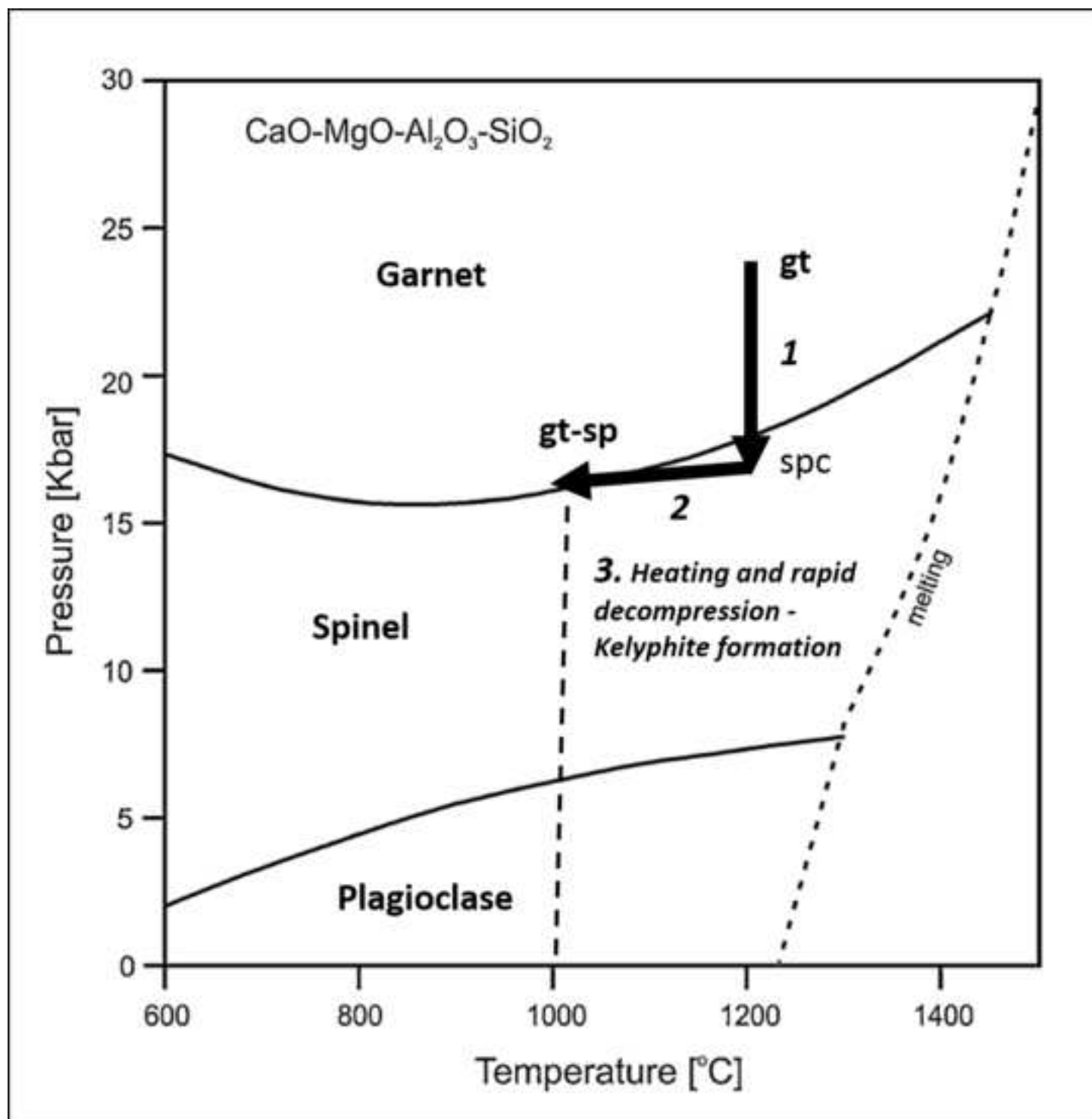




Table 1. Modal mineralogy and nomenclature of garnet peridotites and garnet-spinel peridotites from Pali-Aike and Vitim.

Sample	Thin section					3D volume			
	Ol%	Opx%	Cpx%	Gt%	Sp%	Silicates%	Gt%	Sp%	Rock-type
<i>Pali-Aike</i>									
PA 10	69.2	23.1	1.5	3.5	2.7	98.7	0.7	0.6	Garnet-spinel harzburgite
PA 13	71.2	16.6	1.0	10.7	0.5	97.4	2.5	0.03	Garnet-spinel harzburgite
PA 16	58.2	21.2	11.2	5.8	3.6	97.7	1.9	0.4	Garnet-spinel lherzolite
PA 18	58.9	34.0	1.1	6.0	0.0	90.4	9.6	0.01	Garnet harzburgite
PA 31	75.2	8.1	10.7	5.9	0.2	99.1	0.8	0.1	Garnet-spinel lherzolite
<i>Vitim</i>									
VI 20	54.1	15.4	3.0	26.7	0.8	98.97	0.95	0.08	Garnet-spinel harzburgite
VI 313-116 <sup>i</sup>	66.6	19.7	9.3	4.3	0.1	92.4	7.6	<0.1	Garnet lherzolite
VI 313-148 <sup>ii</sup>	59.5	13.2	6.8	20.5	0.0	67.2	32.3	0.5	Garnet lherzolite
VI 313-532 <sup>iii</sup>	58.1	18.6	17.0	6.3	0.0	90.0	9.8	0.2	Garnet-spinel lherzolite
VI 313-1270	-	-	-	-	-	98.7	1.3	0.0	Garnet lherzolite
VI 313-1280	68.4	16.5	10.8	3.8	0.0	-	-	-	Garnet lherzolite
VI 313-1278	52.4	23.6	9.0	14.2	0.8	-	-	-	Garnet-spinel lherzolite

<sup>i</sup> Thin section shows a gt-sp cluster but 3D volume reveals most grains are sp-free and so sample is characterised as a gt peridotite.

<sup>ii</sup> Thin section lacks sp but 3D volume reveals a single gt-sp cluster and 3D rendered images show small sp blebs not associated with gt distributed through the core. Remaining gt grains are sp-free and so sample is characterised as a gt peridotite.

<sup>iii</sup> Thin section lacks sp but 3D volume reveals the presence of gt-sp clusters. Sample characterised as a gt-sp peridotite based on 3D volume.

Background dataset for online publication only

[Click here to download Background dataset for online publication only: Probe data revised.xlsx](#)

Video P4 13

[Click here to download Video: BM 2004 P4 13 - gt yellow sp red.mp4](#)

**Video P4 18**

**[Click here to download Video: Bm 2004 P4 18 - Gt Yellow Sp Green.mp4](#)**

**Video V 313 116**

**[Click here to download Video: VI 313 116 - gt yellow no sp in cropped core.mp4](#)**

**Video V 313 532**

**[Click here to download Video: VI 313 532 - gt yellow sp red.mp4](#)**

**Video P4 10**

**[Click here to download Video: Bm 2004 P4 10 - Gt blue Sp red.mp4](#)**

# **\*Declaration of Interest Statement**

The authors declare that they have no competing interests.